NEAR-SURFACE HYDROLOGIC RESPONSE FOR A STEEP, UNCHANNELED CATCHMENT NEAR COOS BAY, OREGON: 2. PHYSICS-BASED SIMULATIONS

BRIAN A. EBEL*[†], KEITH LOAGUE*, JOEL E. VANDERKWAAK**,
WILLIAM E. DIETRICH***, DAVID R. MONTGOMERY[§], RAYMOND TORRES[§§],
and SUZANNE P. ANDERSON[‡]

ABSTRACT. The comprehensive physics-based hydrologic-response model *InHM* was used to simulate 3D variably-saturated flow and solute transport for three controlled sprinkling experiments at the Coos Bay 1 (CB1) experimental catchment in the Oregon Coast Range. The *InHM*-simulated hydrologic-response was evaluated against observed discharge, pressure head, total head, soil-water content, and deuterium concentration records. Runoff generation, tensiometric/piezometric response in the soil, pore-water pressure generation, and solute (tracer) transport were all simulated well, based on statistical and graphical model performance evaluation. The *InHM* simulations reported herein indicate that the 3D geometry and hydraulic characteristics of the layered geologic interfaces at CB1 can control the development of saturation and pore-water pressures at the soil-saprolite interface. The weathered bedrock piezometric response and runoff contribution were not simulated well with *InHM* in this study, most likely as a result of the uncertainty in the weathered bedrock layer geometry and fractured-rock hydraulic properties that preclude accurate fracture flow representation. Sensitivity analyses for the CB1 boundary-value problem indicate that: (i) hysteretic unsaturated flow in the CB1 soil is important for accurate hydrologic-response simulation, (ii) using an impermeable boundary condition to represent layered geologic interfaces leads to large errors in simulated magnitudes of runoff generation and pore-water pressure development, and (iii) field-based retention curve measurements can dramatically improve variably-saturated hydrologic-response simulation at sites with steep soil-water retention curves. The near-surface CB1 simulations reported herein demonstrate that physics-based models like *InHM* are useful for characterizing detailed spatio-temporal hydrologic-response, developing process-based concepts, and identifying information shortfalls for the next generation of field experiments. The field-based observations and hydrologic-response simulations from CB1 highlight the challenges in characterizing/simulating fractured bedrock flow at small catchments, which has important consequences for hydrologic response and landslide initiation.

INTRODUCTION

The conceptual understanding of hydrologic response at the hillslope-scale has improved through careful field observations (for example, Cappus, 1960; Whipkey, 1965; Kirkby and Chorley, 1967; Dunne and Black, 1970a, 1970b; Anderson and Burt, 1978) and hydrologic-response simulation (for example, Freeze, 1971, 1972a, 1972b; Beven, 1977, 1978). Despite the considerable progress in recent decades, there are still many unanswered questions in hillslope hydrology such as new-old water (for example, Kirchner, 2003; Cloke and others, 2006; Jones and others, 2006), rapid hydrologic response (Torres and others, 1998; Rasmussen, 2001), and the dynamics of pore-water

*Department of Geological and Environmental Sciences, Stanford University, Stanford, California 94305-2115
**3DGeo Development Inc., Santa Clara, California 95054
***Department of Earth and Planetary Science, University of California, Berkeley, California 94720-4767
[§]Department of Earth and Space Sciences, University of Washington, Seattle, Washington 98195
[§§]Department of Geological Sciences, University of South Carolina, Columbia, South Carolina 29208
[‡]Institute of Arctic and Alpine Research, University of Colorado, Boulder, Colorado 80309-0450
[†] Corresponding author: bebel32@pangea.Stanford.EDU

pressure generation related to landslide initiation (for example, Iverson and others, 2000). Additionally, vigorous debates about process representation in hydrologic modeling continue (for example, Beven, 2000; Loague and VanderKwaak, 2004; Kirchner, 2006).

There are many valuable approaches for examining hydrologic processes. One proven framework for investigating hydrologic response at the field-scale is the measure and model protocol, pioneered in hydrology by Robert E. Horton (see Beven, 2004). A fundamental principle behind Horton's approach is to use observed data to develop, parameterize, and evaluate mathematical models of hydrologic systems. It follows that increasing model complexity demands increasingly large data sets. Not surprisingly, data shortfalls have consistently been an Achilles heel for rigorous, physics-based simulation of hydrologic-response (Loague and VanderKwaak, 2004) and have driven hydrologists towards models with fewer parameters (Beven, 1993, 2006).

The measure and model protocol is frequently utilized to investigate subsurface saturation development, piezometric response, runoff generation, and solute movement at the field-scale. The mathematical models employed span a broad spectrum from relatively simple "pipe and pot" models to parsimonious topographic-index based models to complex, 3D variably-saturated flow models based on Richards equation (see Loague and Vanderkwaak, 2004). Regardless of the model used, the importance of the measure component of the measure and model approach cannot be understated (Sidle, 2006). Field measurements provide both the physical parameter estimates for the flow model and the data for evaluating the simulated versus observed hydrologic response. Most hillslope hydrology modeling efforts limit model performance evaluation to comparing the simulated and observed hydrographs (Vertessy and Elsenbeer, 1999). Several hydrologic-response modeling studies have demonstrated that matching the simulated and observed integrated catchment response (that is, the discharge hydrograph) is no guarantee that the internal, spatially-distributed hydrologic response is correct (Beven, 1997; Wigmosta and Lettenmaier, 1999; Saulnier and Datin, 2004). Ebel and Loague (2006) demonstrated that equifinality (see Beven, 2006) in physics-based hydrologic-response simulation is only tractable when the distributed point responses are used for model performance evaluation.

Many physics-based hydrologic models simulate spatial patterns and dynamics of internal state variables (for example, soil-water content, pore pressure, or solute concentrations). It follows that simulations designed to capture distributed responses should be compared to spatially-distributed observations. For example, evaluation of simulated versus observed saturated areas at the land surface (for example, Ambroise and others, 1996a, 1996b) and at a saturated hydraulic conductivity contrast (for example, Tromp-van Meerveld and McDonnell, 2006) offer an internal check of the simulated catchment response. Comparisons of simulated and observed soil-water contents (for example, Merot and others, 1995; Bronstert and Plate, 1997) also provide feedback on the distributed simulation capabilities of a hydrologic model. Piezometer (for example, Jackson and Cundy, 1992; Lamb and others, 1998; Franks and others, 1998; Dhakal and Sidle, 2004) and tensiometer (for example, Freer and others, 2004) measurements facilitate evaluation of simulated total hydraulic heads. As noted by Beven (1989), comparisons of measured and simulated state variables assume that the point measurements and simulated values result from the same physical processes acting over a similar support volume.

In response to the important hydrologic research contributions from the aforementioned efforts, exhortations for physics-based hydrologic modeling to employ spatially distributed data sets for parameterization and evaluation continue (see Beven 1989, 1993; Vertessy and Elsenbeer, 1999; Grayson and others, 2002; Wealands and others, 2005). The modeling effort reported herein is motivated by the potential benefits of

thoroughly evaluating the distributed hydrologic simulation capability of a physics-based model against the rich data set from the Coos Bay 1 experimental catchment (CB1) in the Oregon Coast Range. A well parameterized physics-based hydrologic-response model could be used to examine the nuances and controlling factors of pore-water pressure development, runoff generation, and water/solute movement and clarify ambiguities in interpretation of hydrologic-response observations (see, for example, Stephenson and Freeze, 1974).

The spatially-distributed, hillslope-scale CB1 hydrologic-response data set is ideal for employing the measure and model approach. The long-term research at CB1 (see Montgomery, ms, 1991; Anderson, ms, 1995; Torres, ms, 1997; Schmidt, ms, 1999) focused on process-based hydrologic response and hillslope geomorphology. Detailed site characterization and hydrologic-response observations from artificial sprinkling and tracer experiments and natural storms were collected at CB1. To the best of the authors' knowledge, the CB1 hydrologic-response data is the most comprehensive for any steep catchment that has experienced slope failure. CB1 offers a rigorous test of the ability of a comprehensive physics-based hydrologic-response model to match the integrated and distributed hydrologic response of a hillslope to controlled sprinkling experiments. However, it was not the intention of this study to meticulously calibrate the model parameters to exactly reproduce all the observed CB1 data. Instead, the model parameters were selected to be faithful to the field measurements and conceptual geologic model from previous CB1 investigations.

The work reported here is the second of a two-part paper, describing comprehensive near-surface hydrologic-response simulations using data analyses from the first paper (Ebel and others, 2007) to parameterize the CB1 boundary-value problem (BVP). It is our opinion that careful and thorough field observation (of the type conducted at CB1) combined with comprehensive physics-based hydrologic-response modeling offers a powerful approach to concept development in hillslope hydrology and hydrogeomorphology.

CB1 STUDY AREA

The 860 m^2 CB1 experimental catchment is a steep ($\sim$43° slope), unchanneled hollow, with a maximum elevation of $\sim$300 m above sea level. The high surface saturated hydraulic conductivity and the permeability contrast between the soil and underlying bedrock favors subsurface stormflow as the primary runoff generation mechanism at CB1 (Torres and others, 1998). Detailed characterization of hydrologic-response at CB1 was facilitated though three carefully controlled sprinkling and tracer experiments (see Anderson and others, 1997a; Montgomery and others, 1997; Torres and others, 1998). Hydrologic-response observations at CB1 were collected during the three experiments from 148 manual rain gages, three automated rain gages, two weirs, 223 piezometers, 100 tensiometers, 42 time-domain reflectometry (TDR) waveguide pairs, and 34 lysimeters (Anderson and others, 1997a, 1997b; Montgomery and others, 1997; Torres and others, 1998).

The potential impacts of instrument emplacement and data collection on the CB1 subsurface were minimized by constructing 14 suspended wooden platforms. The CB1 measurements provide topography, characteristics of the colluvial soil [geometry/ thickness of soil (over 100 soil borings from piezometer installation), saturated hydraulic conductivity (slug tests), soil-water content and porosity (TDR measurements), capillary pressure relationships (from plot experiments)], irrigation rates, weir discharge, pressure head response in the colluvial soil and upper saprolite, tracer concentrations, and discharge chemistry. Figure 1 shows a map of the CB1 instrumentation used for performance evaluation of the hydrologic-response simulations reported herein (note that all operational instruments are used for evaluation of model performance in this study). Further information on the CB1 catchment and the
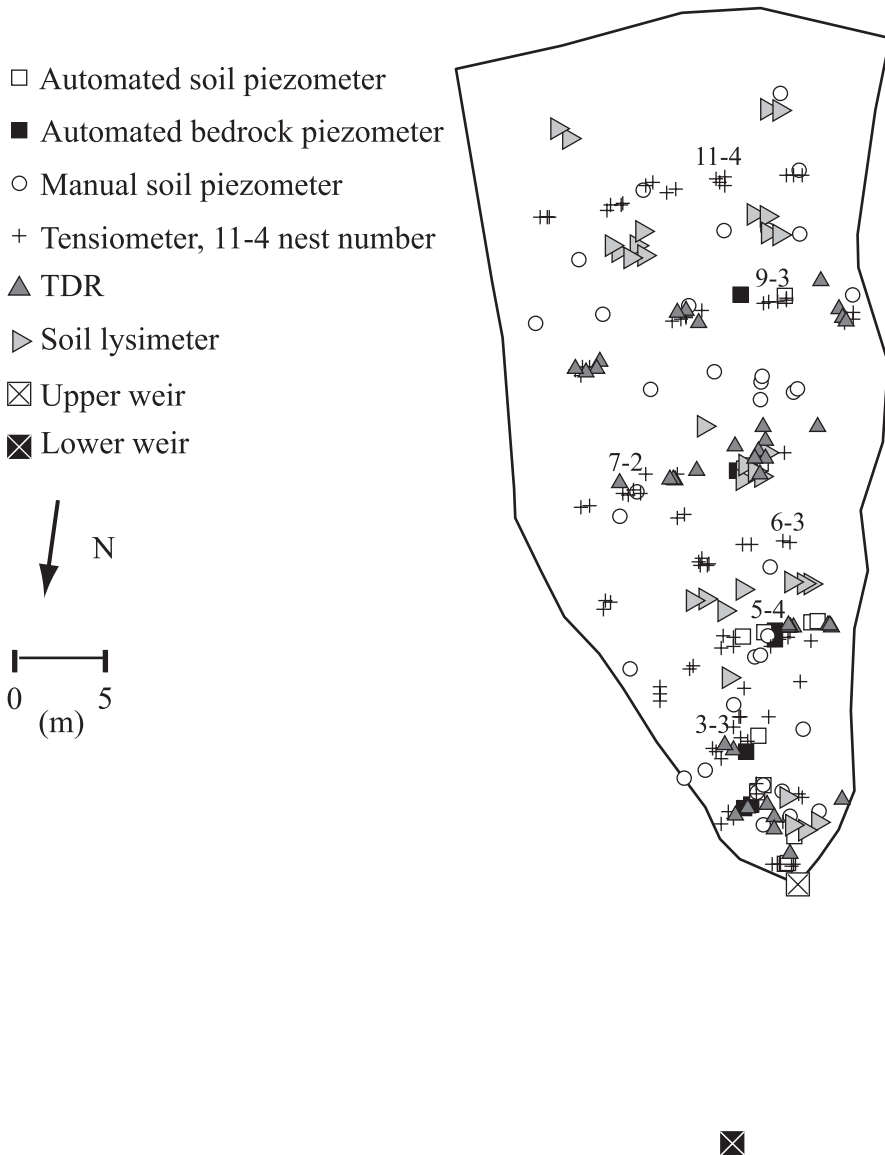
Fig. 1. Locations of the CB1 instrumentation used for model performance evaluation. The tensiometer numbers denote the selected nests shown in figure 10, where the first number is the platform row and the second number is the location (see Ebel and others, 2007 for the platform locations).

long-term monitoring effort at CB1 are available in Montgomery (ms, 1991), Montgomery and others (1997, 2002), Montgomery and Dietrich (2002), Anderson (ms, 1995), Anderson and others (1997a, 1997b), Torres (ms, 1997), Torres and others (1998), and Ebel and others (2007). It is worth mentioning that the CB1 slope failed as a result of a large storm in November, 1996.

CB1 BOUNDARY-VALUE PROBLEM

Simulating the dynamic subsurface hydrologic response of CB1 to rainfall/sprinkling requires solving a BVP, which is a mathematical model of the system (Freeze
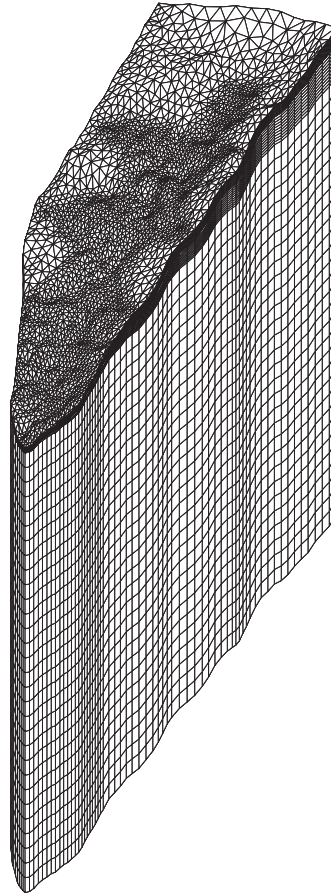
Fig. 2. Finite-element mesh for the CB1 boundary-value problem.

and Cherry, 1979). The mathematical model consists of (i) the partial differential equations describing flow within the system, (ii) a method of solving the governing equations, (iii) the boundary conditions (BCs), (iv) the spatial parameterization of the surface/near- surface hydraulic properties, and (v) the initial conditions (ICs).

The Hydrologic-response Model

The governing equations used to describe flow at CB1, part (i) of the BVP, are Richards equation of 3D variably-saturated flow in the subsurface, the diffusion-wave approximation of the shallow-water equations at the surface, and the advection-dispersion equation for solute transport. Solution of the governing equations, part (ii) of the BVP, utilizes the finite-element method. Figure 2 shows the CB1 finite-element mesh consisting of 264,220 prism elements (138,544 nodes) in the subsurface and 4804 triangular elements (2474 nodes) for the surface. The vertical nodal spacing (Δz) in the CB1 mesh varies from 0.04 m (near surface) to 1.67 m (at depth); the horizontal nodal spacing (Δx, Δy) varies from 0.4 m (downgradient areas, along the measurement platforms, and near the hollow axis) to 2.0 m (near the upgradient boundaries). An adaptive time step (Δt) was used for the hydrologic-response simulations in this study. Parts (i) and (ii) of the BVP comprise the hydrologic-response model. For this effort,

the hydrologic-response model was the comprehensive *Integrated Hydrology Model* (*InHM*), first developed by VanderKwaak (ms, 1999). *InHM* quantitatively simulates, in a fully-coupled approach, 3D variably-saturated flow and solute transport in porous media and 2D flow and solute transport over the surface and in open channels. *InHM* utilizes Newton iteration to implicitly solve one system of discrete equations with spatially variable properties and BCs, requiring no iteration between separate models or model components and no artificial BCs. It is worth noting that *InHM* has no *a priori* assumption of a specific streamflow generation mechanism. *InHM* has been success-fully employed for catchment-scale rainfall-runoff simulations (Vanderkwaak and Loague, 2001; Loague and VanderKwaak, 2002; Loague and others, 2005; Mirus and others, 2007; and Heppner and others, 2007) and for solute transport simulations (Vanderkwaak, ms, 1999; Jones and others, 2006).

Subsurface and surface fluid flow.—Subsurface flow, in 3D variably-saturated porous media is estimated by:

$$\nabla \cdot f^a \, \vec{q} \pm q^b \pm q^e = f^v \frac{\partial \phi S_w}{\partial t} \tag{1}$$

where $\vec{q}$ is the Darcy flux [LT^{-1}], q^b is a specified rate source / sink [T^{-1}], q^e is the rate of water exchange between the subsurface and surface continua [T^{-1}], ϕ is porosity [m^3 m^{-3}], S_w is water saturation [m^3 m^{-3}], t is time [T], f^a is the area fraction associated with each continuum [-], and f^v is the volume fraction associated with each continuum [-]. The Darcy flux is given by:

$$\vec{q} = -k_{rw} \frac{\rho_w g}{\mu_w} \, \vec{k} \nabla(\psi + z) \tag{2}$$

where k_{rw} is the relative permeability [-], ρ_w is the density of water [ML^{-3}], g is the gravitational acceleration [LT^{-2}], μ_w is the dynamic viscosity of water [ML^{-1}T^{-1}], $\vec{k}$ is the intrinsic permeability vector [L^2], z is the elevation head [L], and ψ is the pressure head [L]. The transient flow of water on the land surface is estimated by the diffusion-wave approximation of the depth-integrated shallow water equations. The 2D surface flow is conceptualized as a second continuum that interacts with the underly-ing variably-saturated porous medium through a thin soil layer of thickness a_s [L]. Assuming a negligible influence of inertial forces and a shallow depth of water, ψ_s [L], the conservation of water on the land surface is described by:

$$\nabla \cdot \psi_s^{mobile} \, \vec{q}_s \pm a_s q^b \pm a_s q^e = \frac{\partial (S_{w_s} h_s + \psi_s^{store})}{\partial t} \tag{3}$$

where $\vec{q}_s$ is the surface water velocity [LT^{-1}], q^b is the source/sink rate (that is, rainfall/ evaporation) [T^{-1}], q^e is the surface-subsurface water exchange rate [T^{-1}], a_s is the characteristic length scale for surface/subsurface interaction [L], S_{w_s} is the surface saturation [-], and h_s is the average height of non-discretized surface microtopography [L]. Surface water velocities are calculated utilizing a two-dimensional form of the Manning water depth/friction discharge equation given by:

$$\vec{q}_s = -\frac{(\psi_s^{mobile})^{2/3}}{\vec{n} \Phi^{1/2}} \nabla(\psi_s + z) \tag{4}$$

where $\vec{n}$ is the Manning's surface roughness tensor [TL$^{-1/3}$] and Φ is the friction (or energy) slope [-]. The linkages between the different components of *InHM* are through first-order, physically-based flux relationships driven by pressure-head gradi-ents. Infiltration and exfiltration rates are determined by spatially variable subsurface

properties, spatially and temporally variable subsurface pressure-head gradients, and spatially and temporally variable surface water depths.

Subsurface and surface solute transport.—Subsurface solute transport in a 3D variably saturated porous medium is estimated by:

$$f^v \frac{\partial CR}{\partial t} = -\nabla \cdot f^a \vec{q} C + \nabla \cdot f^a[(\phi S_w \bar{D}_w)\nabla C] \pm q^b(C - C^*) \pm f^v(q^e C^e \pm q^{ed}) \qquad (5)$$

where C is concentration [ML^{-3}], C^* is source concentration [ML^{-3}], $\bar{D}_w$ is dispersion/diffusion (water) coefficient [L^{2}T^{-1}], q^{ed} is the diffusive exchange between continua [MT^{-1}], C^e is the concentration in the upstream continua [ML^{-3}], and R is storage/retardation [-]. The depth-integrated solute transport equation for the surface is given by:

$$\frac{\partial C_s R_s}{\partial t} = -\nabla \cdot \psi_s^{mobile} \vec{q}_s C_s + \nabla \cdot [\psi_s^{mobile} \bar{D}_{ws} \nabla C_s] \pm a_s q_s^b(C - C^*) \pm a_s(q^e C^e + q^{ed}) \qquad (6)$$

where C_s is the surface concentration [ML^{-3}], R_s is surface storage/retardation [-], and $\bar{D}_{ws}$ is the two-dimensional surface dispersion tensor [L^{2}T^{-1}].

Boundary Conditions

The BCs applied to the CB1 catchment are part (iii) of the BVP. *InHM* requires specifying both the surface and subsurface BCs when solving the fully-coupled partial differential equations for surface/subsurface fluid flow. Figure 3 is a schematic of the specified BCs at CB1. Table 1 represents the mathematical expressions for the surface/subsurface flow and transport BCs identified in figure 3.

Surface boundary conditions.—The surface flow BC at the upgradient boundary, AB, is impermeable (drainage divide). Impermeable flow surface BCs are also specified at the sides, AF and BG (drainage divides). A critical depth flow BC (see Chow, 1959; Freeze, 1978) is used to represent the surface flow across the upper weir at the downgradient boundary, FG (the checkerboard-patterned area in fig. 3). The BC applied to the surface, ABHE, is a specified flux (the observed sprinkling rates applied as Kriged snapshots, see Ebel and others, 2007); the sprinkling flux is applied to the planimetric area to be physically consistent with the rain gage orientation. Evapotranspiration during the sprinkling experiments is not included in the flux from the surface boundary condition based on the analysis presented by Ebel and others (2007), which showed that the majority of evapotranspiration occurs before the sprinkling flux reaches the manual rain gages. The surface solute transport BCs are no concentration gradient at the upgradient boundary, AB, and the side boundaries, AF and BG. The downgradient solute transport BC is a back-calculated (that is, upstream weighted) flux, FG. Across the surface, ABHE, the specified concentrations of Deuterium (see Anderson, ms, 1995) are applied with the specified sprinkling flux as a function of time.

Subsurface boundary conditions.—The subsurface BC at the upgradient drainage divide, ABCD, is impermeable. Impermeable subsurface BCs are specified at the sides, BCIH and ADJE. The basal BC, DCIJ, is impermeable; the depth of this boundary was set progressively further away from the near-surface until the BC no longer impacted simulated hydrologic response. The CB1 upper weir (see figs. 1 and 3) consists of sheet metal sealed to the bedrock using concrete and is represented using an impermeable BC. The downgradient BC at the front face of CB1 (except for the upper weir), EHIJ, was set to a local head BC, as described by Heppner and others (2007). The local head BC represents a known hydraulic head value at a point outside the boundaries of the
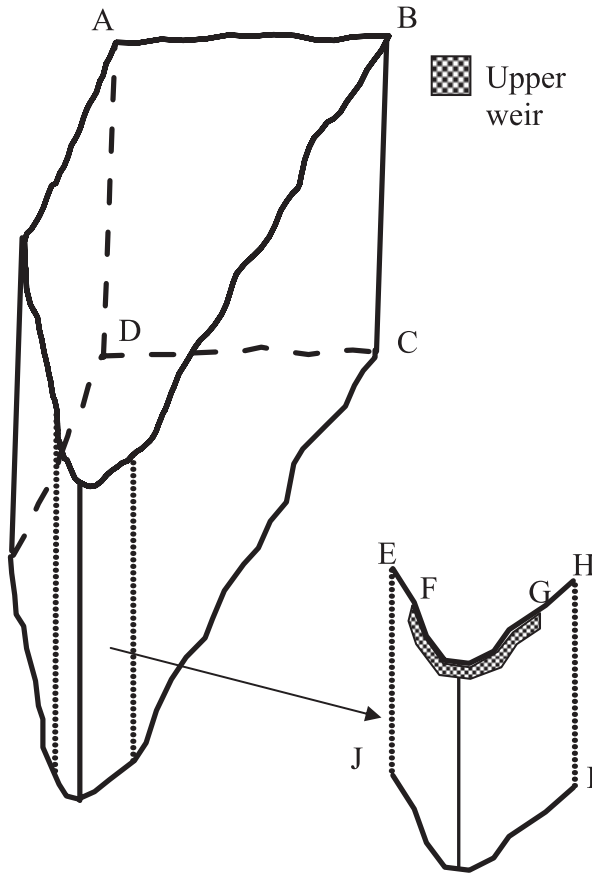
Fig. 3. Boundary condition specification for the CB1 boundary-value problem (also see table 1, not to scale).

finite-element mesh. For boundary nodes assigned the local head BC, the volumetric boundary flux ($Q_{b,l}$) [L^3T^{-1}] is calculated as:

$$Q_{b,l} = k_{rw} \frac{\rho_w g}{\mu_w} \vec{q} \, A \frac{(h_l - h_{b,pm})}{dl} \qquad (7)$$

where h_l is the total head at the local head point [L], $h_{b,pm}$ is the total head for the porous medium equation at the boundary node [L], A is the nodal area [L2], and dl is the (positive) distance in the x-y plane between the node and the regional sink point [L]. Because the *InHM* solution to the subsurface/subsurface flow equations is fully coupled, the water and solute fluxes between the subsurface and surface continua are not specified *a priori*, and instead depend on dynamic pressure-head gradients. The solute transport BCs for the subsurface are no concentration gradient at the upgradient boundary, ABCD, the side boundaries, BCIH and ADJE, and the basal boundary, DCIJ. The downgradient solute transport BC is a back-calculated (that is, upstream weighted) flux across the front face, EHIJ.

Spatial Parameterization of Hydrogeologic Layer Properties

Part (iv) of the BVP consists of parameterizing the hydraulic properties of the hydrogeologic units. Figure 4 shows the hydrogeologic units used to parameterize the

TABLE 1

Boundary conditions for the CB1 boundary-value problem

Boundary [1]	Flow		Solute transport	
	Surface	Subsurface	Surface	Subsurface
AB	$\partial h / \partial x_i = 0$		$\partial C / \partial x_i = 0$	
AF	$\partial h / \partial x_i = 0$		$\partial C / \partial x_i = 0$	
BG	$\partial h / \partial x_i = 0$		$\partial C / \partial x_i = 0$	
FG	critical depth		BCF [2]	
ABHE	$q^b(x_i) = q^b(x_i,t)$		$C = C(t)$	
ABCD		$\partial h / \partial x_i = 0$		$\partial h / \partial x_i = 0$
BCIH		$\partial h / \partial x_i = 0$		$\partial h / \partial x_i = 0$
ADJE		$\partial h / \partial x_i = 0$		$\partial h / \partial x_i = 0$
DCIJ		$\partial h / \partial x_i = 0$		$\partial h / \partial x_i = 0$
Upper weir		$\partial h / \partial x_i = 0$		$\partial h / \partial x_i = 0$
EHIJ		local head		BCF [2]

[1] see figure 3
[2] BCF is a back-calculated flux based on the concentration at the upstream finite-element nodes

subsurface at CB1. The hydrogeologic model presented in figure 4 is adapted from Anderson and others (2002). Table 2 contains the hydrogeologic parameters for the CB1 subsurface. The soil and saprolite depths (see fig. 4) were interpolated using ordinary Kriging of 630 measured soil and saprolite depths (over 100 are in and around the CB1 BVP) from the Mettman Ridge area (Montgomery and others, 1997; Schmidt, ms, 1999). The weathered bedrock depths are estimated from the deep drill core at the ridge crest and 11 borings into the weathered bedrock associated with the bedrock piezometer installation (Anderson and others, 2002; Montgomery and others, 2002). Core recovery was low (0 – 30%) in these borings and there is considerable uncertainty in the weathered bedrock layer thicknesses at CB1 (Anderson, ms, 1995). The weathered bedrock layer thickness thins downslope (Anderson, ms, 1995), with a thickness of 4 m at the ridgecrest (constrained by the deep drill core) and near-zero thickness near the upper weir. The fractured bedrock layer described in Anderson and others (2002) is incorporated into the bedrock layer in figure 4. The depth of the bedrock layer extends to the basal boundary, DCGH in figure 3.

Hydrogeologic layer porosities.—Soil porosity is estimated as the mean water content at saturation (0.5 m³ m⁻³) from the six retention curve experiments of Torres and others (1998), which is the same value reported from CB1 by Montgomery and others (2002). The porosity estimated from the retention curve experiments is less than estimates from soil pits (0.6 and 0.7 m³ m⁻³) at a nearby catchment by Anderson and others (2002) and Anderson and others (1997a), respectively. Porosities for the saprolite, weathered bedrock, and bedrock layers (see table 2) were estimated from the CB1 drill core data from Anderson and others (2002).

Hydrogeologic layer hydraulic conductivities.—Saturated hydraulic conductivities for the CB1 layers were parameterized using reanalysis of 185 falling head slug tests (see Ebel and others, 2007) and incipient-ponding sprinkling rates at the surface during the retention-curve experiments of Torres and others (1998). Spatially uniform hydraulic conductivities are used within each of the hydrogeologic layers (see fig. 4 and table 2) because there are insufficient data to characterize the spatial structure for a meaningful 3D interpolation (see Ebel and others, 2007). The surface saturated
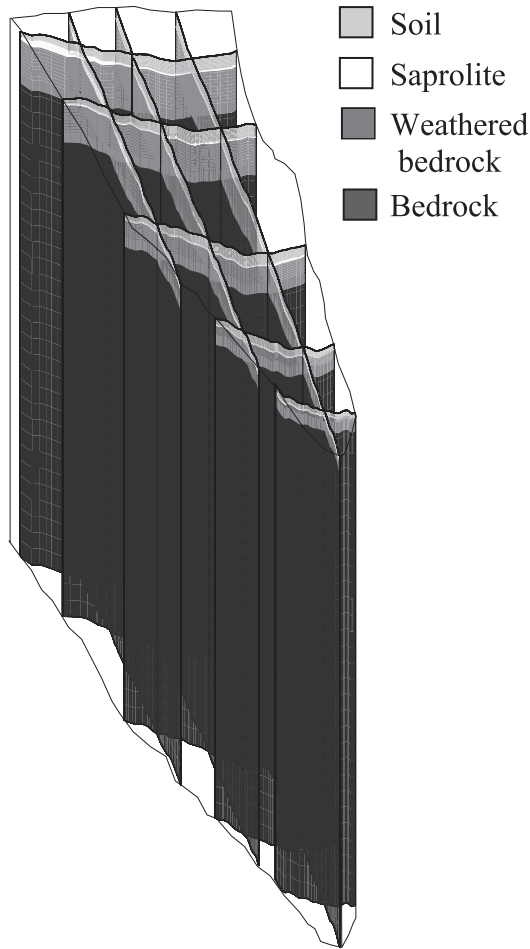
Fig. 4. Fence diagram of the hydrogeologic layers used to parameterize the CB1 subsurface.

hydraulic conductivity is estimated using the sprinkling rates at incipient ponding (after the total head gradient becomes unity between two nested tensiometers and the pressure heads are equal to zero) from the retention-curve experiments at CB1 (see Torres and others, 1998). The mean surface saturated hydraulic conductivity from four retention-curve experiments (sprinkling rates were not measured for two of the six retention-curve experiments) is 5.7×10^{-4} m s^{-1}. The arithmetic mean of the slug tests in the soil, which is biased towards deeper measurements, is 1.1×10^{-4} m s^{-1} (Ebel and others, 2007). The arithmetic mean of the aforementioned estimates of surface and subsurface saturated hydraulic conductivities, 3.4×10^{-4} m s^{-1}, is used to represent the saturated hydraulic conductivity of the colluvial soil at CB1. The arithmetic mean of the saturated hydraulic conductivites estimated from CB1 slug tests (see Ebel and others, 2007) within the saprolite (7.2×10^{-5} m s^{-1}) layer provides the estimate used in this study (see table 2). Weathered bedrock saturated hydraulic conductivity estimates from slug tests range over nearly four orders of magnitude with no discernable spatial pattern (Montgomery and others, 2002; Ebel and others, 2007). Because of the uncertainty in the weathered bedrock saturated conductivity estimates and the spatial

Hydrogeologic properties of the CB1 boundary-value problem

Layer [1]	Thickness (m)	Porosity ($m^3 \, m^{-3}$)	Saturated hydraulic conductivity ($m \, s^{-1}$)	Compressibility ($ms^2 kg^{-1}$)
Soil	0.04 - 1.5 [2]	0.50 [4]	3.4×10^{-4} [6]	1×10^{-8} [8]
Saprolite	0.02 - 1.1 [2]	0.15 [5]	7.2×10^{-5} [7]	1×10^{-9} [8]
Weathered bedrock	0.02 - 4.0 [3]	0.15 [5]	5.0×10^{-7}	1×10^{-9} [8]
Bedrock	50	0.12 [5]	5.0×10^{-7}	1×10^{-9} [8]

[1] see figure 4;
[2] Kriged from 630 data points (Schmidt, ms, 1999), including the CB1 piezometer installation;
[3] from Anderson (ms, 1995);
[4] estimated from the retention curves of Torres and others (1998);
[5] estimated from figure 3 in Anderson and others (2002);
[6] arithmetic mean of the surface and subsurface mean estimates;
[7] arithmetic mean from 37 slug tests (see Ebel and others, 2007);
[8] Freeze and Cherry (1979)

bias (sampled along the hollow axis), the conductivities for the weathered bedrock and the bedrock are set to be the same. Slug tests were not conducted in the unweathered CB1 bedrock, so the unweathered bedrock saturated hydraulic conductivity was estimated (via calibration) to be 5.0×10^{-7} m s^{-1}. The calibration range was constrained between 4.0×10^{-7} and 5.0×10^{-7} m s^{-1}, which was the range of unweathered bedrock saturated hydraulic conductivity estimates determined from the rate of water table decline in the deep well during the summer dry season.

    Hydrogeologic layer soil-water retention curves and hydraulic conductivity functions.—*In situ* soil-water retention curves for the soil were measured, using TDR and nested tensiometers, during the six plot experiments conducted by Torres and others (1998). Figure 5A shows the measured soil-water retention data from the six plot experiments and the estimated soil-water retention curve using the van Genuchten (1980) method. Figure 5B shows the hydraulic conductivity function estimated using the van Genuchten (1980) method. Hysteresis is observed in the measured CB1 soil-water retention curves (fig. 5A) at CB1 (Torres and others, 1998) and has been measured at other field sites with sandy soils (for example, Royer and Vachaud, 1975). Some of the CB1 field measurements of hysteretic capillary-pressure relationships were made at unsteady flow conditions, which can cause overestimates of soil-water contents during drying and underestimates of soil-water contents during wetting (Jaynes, 1990). Hysteretic scanning curves in the CB1 soil were represented using the models of Kool and Parker (1987) and Scott and others (1983). The retention curves and hydraulic conductivity functions for the saprolite, weathered bedrock, and bedrock layers were not measured at CB1 and are parameterized using the van Genuchten parameters (that, is α equal to 4.3 m^{-1} and *n* equal to 1.25) from Wu and others (1999) and are not hysteretic.

    Solute transport parameters.—The CB1 subsurface solute transport parameters were not well characterized and consequently are selected from literature values. The longitudinal dispersivity in the subsurface was chosen from figure 5.2 in Gelhar (1993) to be 5.0 m and the two transverse dispersivities were set to one tenth of the longitudinal dispersivity, 0.5 m (S. Gorelick, personal communication, 2001). Deuterium is considered a conservative tracer in this study.
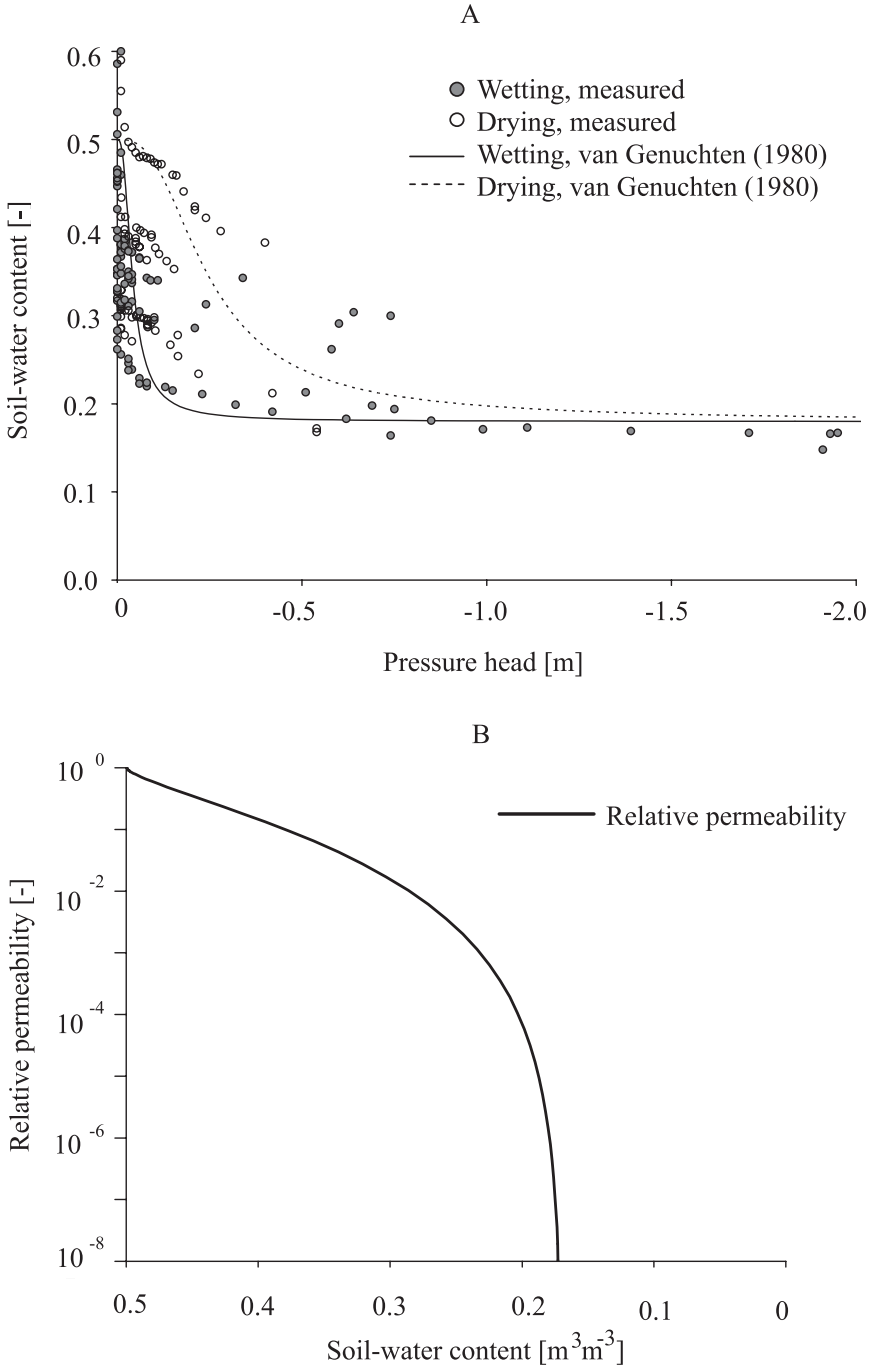
A

B

Fig. 5. Characteristic curves for the CB1 soil. (A) Hysteretic soil-water retention curve data (after Torres and others, 1998) and the estimated soil-water retention curve using the van Genuchten (1980) method. (B) Estimated hydraulic conductivity function using the van Genuchten (1980) method.

Initial Conditions

Part (v) of the CB1 BVP is the ICs. Initial pressure heads for flow simulation and concentrations for solute transport simulation are prescribed at every node in the finite-element mesh. The ICs were determined using the setting up period approach of Binley and Beven (1992) whereby two months of precipitation data (from the automated rain gages at CB1) were used to drive non-hysteretic hydrologic-response simulation preceding experiments 1 and 3 using the wetting curve in figure 5A. The setting up period hydrologic simulations were stopped before the CB1 sprinkling tests that preceded sprinkling experiments 1 and 3. The sprinkling tests were then simulated with the hysteretic soil-water retention curve shown in figure 5A, using ICs gleaned from the setting up period. Pressure heads from the end of hysteretic sprinkling test simulations provide the ICs for sprinkling experiments 1 and 3. The experiment 2 ICs were generated using a setting up period (with hysteresis) starting at the end of experiment 1 and applying measured natural rainfall and sprinkling test rates until the start of experiment 2. Evapotranspiration was not considered during the generation of ICs.

Solute transport simulation requires specifying initial concentrations for every node in the finite-element mesh. There are insufficient δD values from the subsurface lysimeters before sprinkling experiment 3 to estimate subsurface initial δD concentrations throughout CB1. The mean of the δD values from the upper and lower weir one hour before the start of sprinkling experiment 3 was -45.4 permil (δD value relative to Standard Mean Ocean Water, SMOW). The -45.4 permil δD concentration from the upper and lower weir records was used as an estimate for a spatially uniform δD for the entire CB1 surface and subsurface.

The importance of ICs for accurately simulating event-based hydrologic response has been demonstrated by many studies (see, for example, Grayson and others, 1992, 1995; Coles and others, 1997). Approaches for generating initial conditions include treating them as a freely adjustable parameter for different simulations (Coles and others, 1997), utilizing a topographic index to estimate initial soil-water content (Grayson and others, 1992), employing interpolated observed soil-water contents (Merz and Plate, 1997), using a hydrologic-response model to simulate draining the catchment from near saturation (Loague and others, 2005), and the setting up period approach of Binley and Beven (1992). Comparison of *InHM* simulated pressure heads and soil-water contents to the observed values at the start of the CB1 sprinkling experiments supports the use of the setting up period approach for event-based simulations.

EVENT-BASED HYDROLOGIC-RESPONSE SIMULATIONS

Evaluation of Hydrologic-Response Simulations

Proper evaluation of a distributed, transient hydrologic-response model requires observations with high spatial and temporal resolution (see, for example, Vertessy and Elsenbeer, 1999; Wigmosta and Lettenmaier, 1999; Ebel and Loague, 2006). The CB1 upper weir discharge is evaluated against the discharge across the downgradient surface BC (FG in fig. 3). The CB1 lower weir discharge is evaluated against the subsurface flux across the boundary EFGH (see fig. 3) to the estimated depth of the bedrock flowpath contributing to the upper weir. The depth of the area contributing to the lower weir discharge includes the top 5 m of the bedrock layer, corresponding to the approximate depth of the fractured bedrock layer at CB1 (Anderson and others, 2002). Simulated and observed deuterium concentrations at the upper weir are also compared. Tensiometers, piezometers, and lysimeters at CB1 (see fig. 1) are considered point responses and the closest finite-element node is compared for each observation location. The elevation head from the closest finite-element node is used

to calculate total head for both observed and simulated for tensiometers and piezometers. Simulated negative pressure heads are set to zero when compared against observed pressure heads from piezometer records (that is, comparing a negative simulated pressure head at a node against an observed pressure head from a piezometer, which cannot record negative values, is inappropriate). The soil-water content observations from TDR represent the integrated water content along the length of the waveguides, which are inserted vertically into the soil, and are compared against the mean soil-water content for the nearest finite-element nodes from the surface to the waveguide depth.

Model performance is evaluated both statistically and graphically in this study. One measure of model performance used to test *InHM* is the Nash and Sutcliffe (1970) modeling efficiency (*EF*). The expression for *EF* is (James and Burges, 1982; Loague and Green, 1991):

$$EF = \left[\sum_{i=1}^{n} (O_i - \bar{O})^2 - \sum_{i=1}^{n} (P_i - O_i)^2 \right] \Bigg/ \sum_{i=1}^{n} (O_i - \bar{O})^2 \qquad (8)$$

where P_i are the predicted values, O_i are the observed values, n is the number of samples, and $\bar{O}$ is the mean of the observed data. The *EF* statistic ranges from 1.0 to -∞. When the observed and simulated values are identical the *EF* is 1.0. When the *EF* is less than zero, the observed mean is a better predictor of the observed data than the model. An additional measure of model performance is the mean absolute bias (*MAB*) (M. Kirkby, personal communication, 2005):

$$MAB = \frac{\sum_{i=1}^{n} |(O_i - P_i)|}{n} \qquad (9)$$

The results of the CB1 hydrologic-response simulations for the three sprinkling experiments are presented in F6–17 and tables 3–7. Comparison of observed versus simulated hydrologic-response is separated into the integrated response, which included the discharge and deuterium concentrations at the weirs, and the distributed response, which is comprised of the tensiometer, piezometer, TDR, and lysimeter data.

Integrated Response Results

Upper weir discharges.—Figures 6A, 6B, and 6C show the automated stage-recorder observed and *InHM* simulated upper weir discharges for the three CB1 sprinkling experiments. Table 3 presents the model performance and summary statistics for the *InHM* simulated upper weir discharges for the three sprinkling experiments. Based on figure 6 and table 3, *InHM* simulated the upper weir discharges reasonably well for the three sprinkling experiments, especially considering the small observed discharge magnitudes. Examination of figures 6A, 6B, and 6C reveals that the rising limb of the simulated upper weir hydrograph is delayed relative to the observed hydrograph for all three sprinkling experiments. Figures 6A, 6B, and 6C also show that the falling limb of the simulated upper weir hydrograph drains slower than the observed hydrograph for all three sprinkling experiments. The model performance (*EF*) values from table 3 for the simulated upper weir discharges are all greater than zero, with experiment 3 having the best *EF* and experiment 2 having the worst *EF*. The CB1 performance statistics reported in table 3 are similar to what has been previously reported for physics-based hydrologic-response simulations (for example, Loague and others, 2005). Peak simulated discharges are underestimated for experiments 1 and 3 and overestimated for experiment 2 while the timing to peak discharge is underestimated for experiment 1 and overestimated for experiments 2 and 3. Despite the large differences
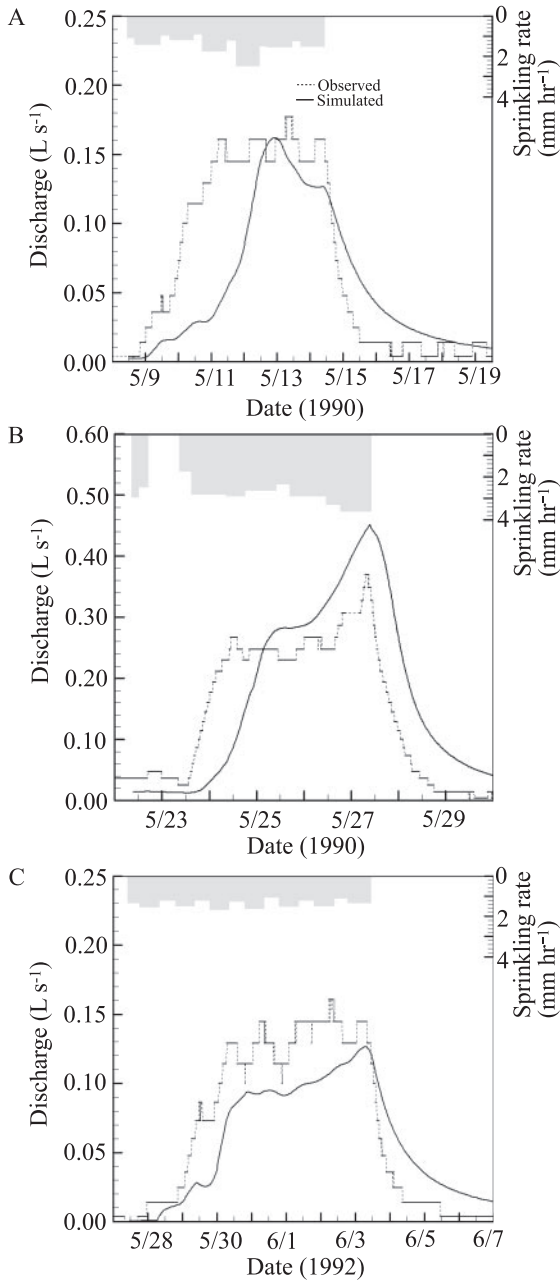
Fig. 6. Observed (see Montgomery and others, 1997; Montgomery and Dietrich, 2002) and simulated discharge hydrograph at the CB1 upper weir and mean sprinkling rate hyetograph. (A) Sprinkling experiment 1. (B) Sprinkling experiment 2. (C) Sprinkling experiment 3.

Model performance, peak, and time to peak for observed versus InHM simulated discharges at the CB1 weirs[1]

Experiment number	Weir	EF^3	Peak discharge (Ls^{-1})			Time to peak discharge (days) [2]		
			Observed	Simulated	Percent difference	Observed	Simulated	Percent difference
1	UW[4]	0.53	0.18	0.16	11.1	4.97	4.43	10.9
2	UW[4]	0.33	0.37	0.45	-22.2	4.97	5.01	-0.8
3	UW[4]	0.71	0.16	0.12	25.0	5.86	6.92	-18.1
3	UW[5]	0.69	0.16	0.12	25.0	5.97	6.92	-15.9
3	LW[4]	<0	0.19	0.03	84.2	2.84	6.04	-112.7

UW is the upper weir, LW is the lower weir
[1]see figure 1 for the weir locations;
[2]time to peak relative to the start of the sprinkler experiment;
[3]modeling efficiency;
[4]evaluated against the automated stage-discharge data;
[5]evaluated against hand-recorded discharge

in temporal resolution between the automated stage-recorder discharge and the manually-recorded discharges from experiment 3, the performance statistics comparing the simulated discharge to the two different observed upper weir discharges in table 3 are nearly identical. Small temporal scale fluctuations in the observed discharge are not captured in the simulated discharges in figures 6A, 6B, and 6C, potentially because of the limited temporal resolution of the applied kriged sprinkling snapshots (see Ebel and others, 2007). The initial discharges are well simulated by *InHM* for all three sprinkling experiments in figures 6A, 6B, and 6C, suggesting that the ICs have been simulated reasonably well using the setting up period approach.

Deuterium concentrations in the upper weir discharge.—Figure 7 presents the integrated CB1 hydrologic-response as observed and simulated δD values in the upper weir discharge during sprinkling experiment 3. Examination of figure 7 indicates that the simulated δD matches the timing of observed deuterium breakthrough very well at the upper weir during experiment 3. It is also clear from figure 7 that the simulated peak δD (-20.9 ‰) is overestimated relative to the observed peak (-29.7 ‰).

Distributed Response Results

Tensiometers and piezometers.—Figures 8A, 8B, and 8C show observed versus simulated pressure heads from tensiometers during the three sprinkling experiments. The results in figure 8 are color coded by time to facilitate separation of model performance throughout the duration of each sprinkling experiment. For interpretation of figures 8A, 8B, and 8C, it is worth noting that the blue scatter points represent IC and early time tensiometer measurements, light blue and green scatter points represent the middle and near the end of the sprinkling, yellow scatter points represent measurements immediately after the sprinkling ends, and red and orange scatter points represent drying conditions after the sprinkling experiments. It is clear from figures 8A and 8C that there are some inaccuracies in the ICs, with the simulated blue scatter points lying to the left of the 1:1 line, indicating that the simulated pressure heads are too large for the IC. For example, the horizontal linear feature in figure 8C of light blue dots near -0.08m simulated pressure head represent tensiometers where the simulated pressure head has risen to the quasi-steady value head but the observed pressure head is still increasing towards the quasi-steady value. In particular, the extremely dry ICs (large negative pressure heads) for experiment 3 are not well
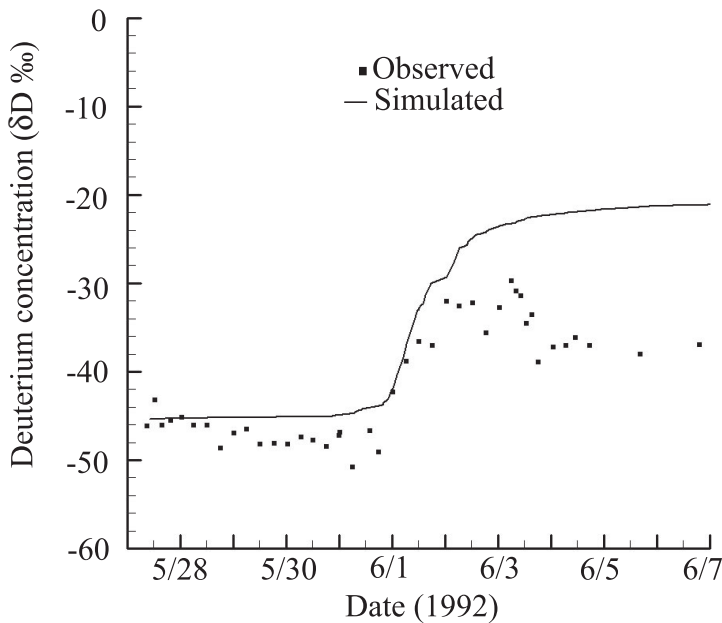
Fig. 7. Observed and simulated deuterium concentration at the CB1 upper weir for sprinkling experiment 3.

represented by the setting up period approach employed in this study. The dry conditions preceding experiment 3 combined with neglecting evapotranspiration during the setting up period may help explain why the ICs are not represented well. Figure 8B shows that the ICs for experiment 2 are more accurately captured because sprinkling experiment 2 followed only one week after experiment 1. Examination of figures 8A, 8B, and 8C shows that the CB1 pressure heads are well simulated during the middle to the end of sprinkling for all three experiments, although the simulated pressure heads are slightly less than the observed pressure heads for all the sprinkling experiments during the middle of the sprinkling experiments. The simulated pressure heads during the draining portion of the three experiments is represented well by the hysteretic simulations, although the simulated draining pressure heads are slightly higher than the observed pressure heads for experiments 1 and 3.

Table 4 presents model performance evaluations for simulated tensiometers during the three sprinkling experiments. The results in table 4 are separated into performance statistics for all the tensiometers deployed during a given sprinkling experiment and only those tensiometers that exhibited positive *EF* values. Examination of table 4 demonstrates that the pressure heads are simulated well for all three sprinkling experiments. Tensiometer *MAB* values are smaller (closer to the observed) for experiments 1 and 2 compared to experiment 3, primarily because of the errors in the simulated ICs for experiment 3. Median *EF* values are better for experiments 1 and 3 when all the tensiometers are considered, but mean *EF* values are better for experiment 2 when only the positive *EF* tensiometers are considered, illustrating the effect of a few very poorly simulated tensiometers in biasing the *EF*. For example, because the range for *EF* is -∞ to 1, a few poorly simulated tensiometers (for example, the *EF* for tensiometer 0-2A during experiment 3 was -106) can result in a mean *EF*
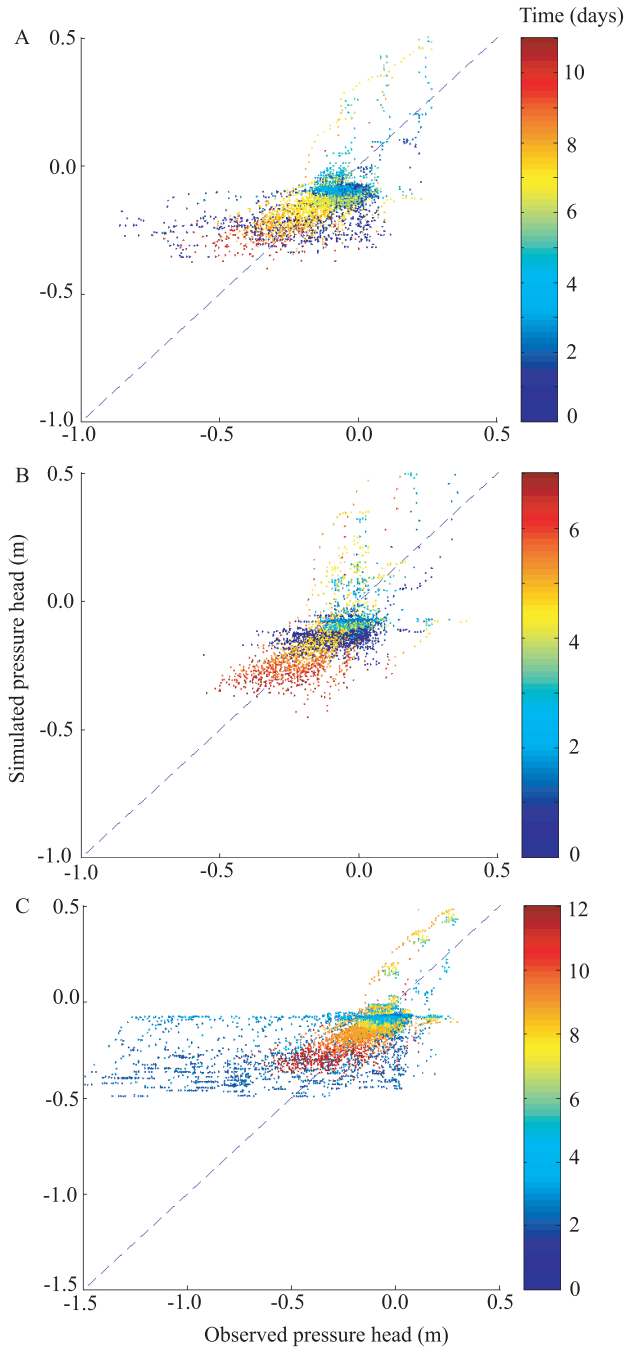
Fig. 8. Simulated versus observed pressure heads from tensiometers color-coded by time from the start of the sprinkling experiment. (A) Sprinkling experiment 1. (B) Sprinkling experiment 2. (C) Sprinkling experiment 3.

Model performance for observed versus InHM simulated pressure heads from the CB1 tensiometers[1]

Experiment number	Number of observations[3]	All tensiometers		Positive *EF* tensiometers[2]			
		Mean		Median		Mean	
		EF[4]	*MAB*[5]	*EF*	*MAB*	*EF*	*MAB*
1	100	<0	0.08	0.28	0.07	0.45	0.07
2	99	<0	0.08	0.02	0.07	0.58	0.06
3	101	<0	0.13	0.32	0.11	0.44	0.12

[1]see figure 1 for the tensiometer locations;
[2]statistics for the tensiometers with *EF* values greater than 0 (61 for experiment 1, 50 for experiment 2, and 73 for experiment 3);
[3]tensiometers were retired and added between the three sprinkling experiments;
[4]modeling efficiency;
[5]mean absolute bias (m)

below zero. This explains why the mean *EF* values from all the tensiometers in table 4 are negative for all three experiments.

The number of positive *EF* tensiometers, relative to the total number deployed, is best for experiment 3 (73) and worst for experiment 2 (50); there are 61 positive tensiometer *EF* values during experiment 1. The difference between the number of positive *EF* tensiometers for the three sprinkling experiments is partially an expression of the ICs. For example, the much drier ICs during experiment 3 provide a larger range in the observed pressure head values. The larger range in observed pressure head causes the mean observed pressure head value to be a worse predictor of the observed pressure heads at a given time, which improves the *EF* values for the simulated pressure heads. Examination of the small differences in the *MAB* for all the tensiometers and only the positive *EF* tensiometers indicates that the *MAB* is a more robust performance statistic than the *EF* for the CB1 tensiometers.

Figures 9A and 9B show contour maps of interpolated performance statistics for *InHM* simulated tensiometers during sprinkling experiment 3. Only positive *EF* values were included in figure 9A and the mean *EF* values for each tensiometer nest (that is, co-located tensiometers emplaced at different monitoring depths) were interpolated. All the tensiometers were included in the mean *MAB* values for each tensiometer nest used to create figure 9B. It is clear that the areas of high *EF* and small *MAB* in figures 9A and 9B correspond well, with a few minor differences resulting from the exclusion of negative *EF* values. Figures 9A and 9B indicate that measured pressure heads are reproduced well by *InHM* in the interior of CB1, especially along the hollow axis. Errors in simulated pressure heads are largest near the CB1 boundaries, in particular near the down gradient BC.

Figure 10 presents total head time series at selected tensiometer nests during sprinkling experiment 3. The selected tensiometer nests were chosen to represent a spatial distribution throughout CB1 and are neither the best nor the worst simulated tensiometers. Table 5 gives the model performance statistics for the selected tensiometers shown in figure 10. Figure 10 and table 5 are organized in a progression from the upgradient boundary (tensiometer nest 11-4 shown in fig. 10A) towards the downgradient boundary (tensiometer nest 3-3 shown in fig. 10F). Examination of figures 10A-F and table 5 demonstrates that the *InHM* simulated subsurface total heads match the temporal patterns and total head magnitudes observed at the CB1 tensiometers during sprinkling experiment 3. All the simulated ICs are too wet relative to the observed, with the exception of some of the deeper tensiometers in nest 9-3 (fig. 10B) and 3-3 (fig.
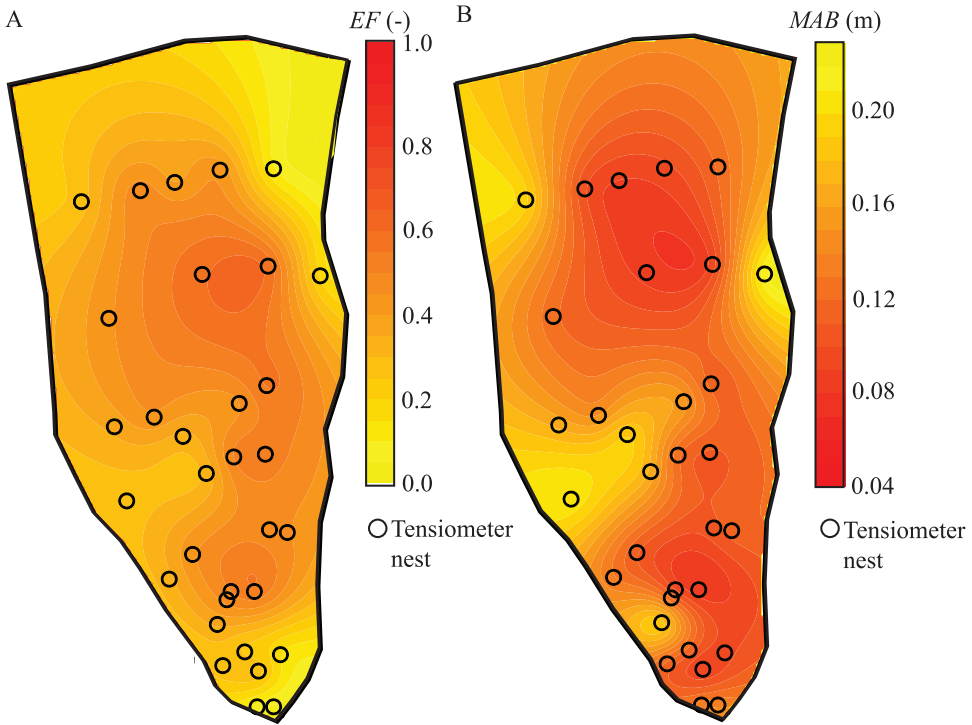
Fig. 9. Interpolated maps of model performance evaluation statistics averaged for each of the 32 CB1 tensiometer nests. (A) *EF*, using only positive values. (B) *MAB*, using all the *MAB* values.

10F), which is consistent with the experiment 3 ICs shown in figure 8C. The drop in simulated tensiometric response in figure 10F results from local variations in sprinkling rates, which are nearly a factor of four larger than the mean sprinkling rate beginning on 5/29/92 and then decline to near the mean sprinkling rate after 5/30/92. The timing of tensiometric response and the rise to a quasi-steady state total head are well simulated by *InHM*, as shown by figures 10A-F. The simulated drying limbs of the tensiometer time series are good overall, although the simulated total heads do not decline fast enough for nests 7-2 (fig. 10C) and 5-4 (fig. 10E). The peak total heads are best simulated in the deeper and middle depth tensiometers and underestimated for the shallower tensiometers. The slight diurnal variations in total head in figure 10 are captured by *InHM*, albeit somewhat damped relative to the observed total heads, because of the limited temporal resolution of the applied sprinkling flux BC that reduces the diurnal variation in applied sprinkling rates (see Ebel and others, 2007).

Table 6 gives the model performance statistics for the simulated CB1 soil/ saprolite and bedrock piezometers during the three sprinkling experiments. Simulated saturation in the CB1 piezometers was best for experiment 2 and worst for experiment 3. The automated pressure-transducer piezometers were better simulated than the hand recorded piezometers in terms of saturation. The *MAB* for the simulated pressure head in the CB1 piezometers is similar to what was reported for the simulated tensiometers in table 4. Based on the *MAB* in table 6, the pressure heads were best simulated for experiment 1 and simulated the worst for experiment 2. Minimal differences in the *MAB* comparing the model performance relative to the automated
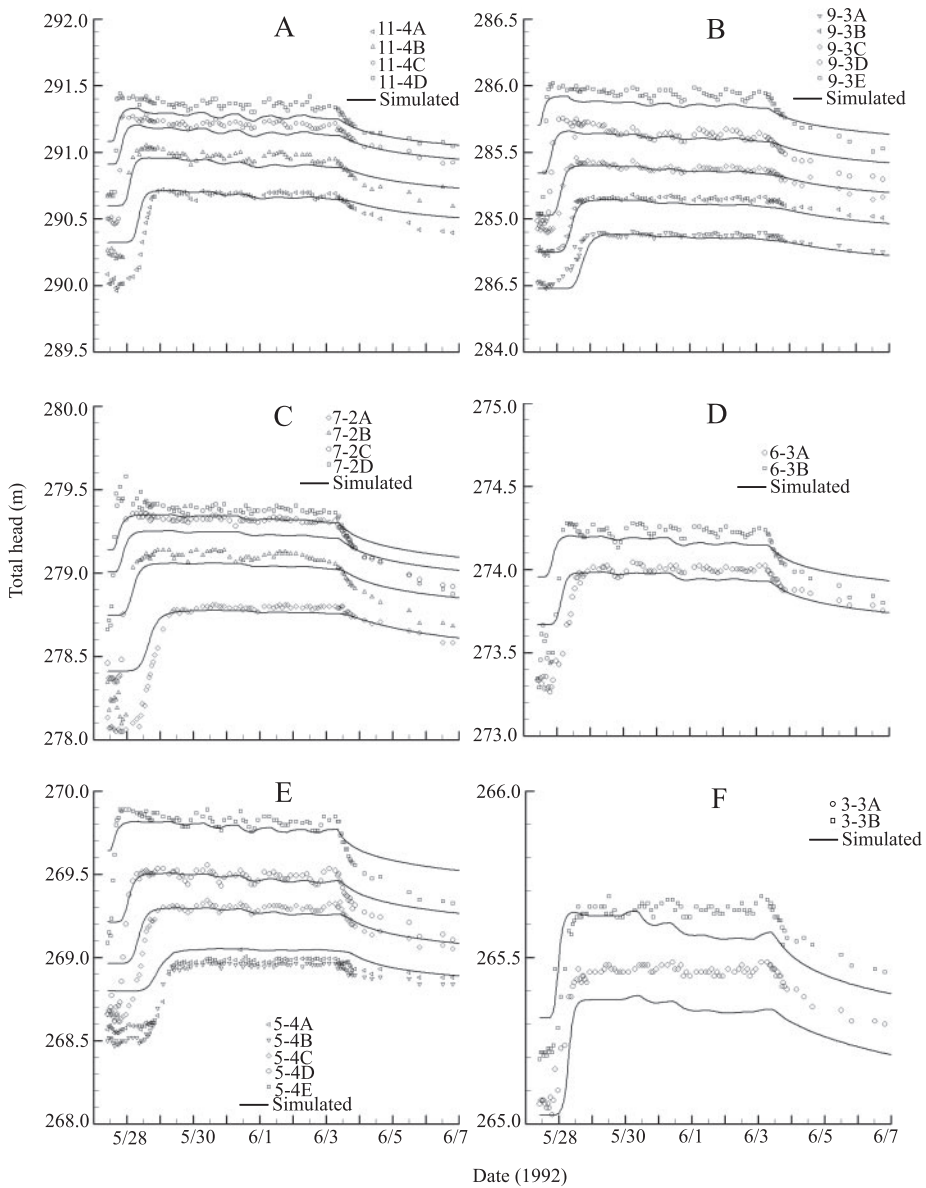
Fig. 10. Simulated and observed tensiometer total head time series from sprinkling experiment 3. Tensiometer nest locations are shown in figure 1. (A) Tensiometer nest 11-4. (B) Tensiometer nest 9-3. (C) Tensiometer nest 7-2. (D) Tensiometer nest 6-3. (E) Tensiometer nest 5-4 (note that 5-4A and B are represented by the same simulated observation point). (F) Tensiometer nest 3-3.

and manual piezometers are shown in table 6 for all three sprinkling experiments. The bedrock piezometers were only deployed at CB1 during experiment 3 and are not simulated well by *InHM*, although the bedrock piezometer saturation is simulated correctly (see table 6).

TABLE 5

Model performance statistics for the selected tensiometers shown in figure 10[1]

Tensiometer[2]	EF[3]	MAB[4]	Tensiometer	EF	MAB
11-4A	0.63	0.09	7-2C	0.42	0.15
11-4B	0.56	0.11	7-2D	0.51	0.09
11-4C	0.55	0.09	6-3A	0.59	0.10
11-4D	0.46	0.10	6-3B	0.43	0.12
9-3A	0.76	0.04	5-4A	0.40	0.11
9-3B	0.92	0.04	5-4B	0.17	0.15
9-3C	0.91	0.03	5-4C	0.67	0.08
9-3D	0.64	0.08	5-4D	0.51	0.09
9-3E	0.34	0.11	5-4E	0.53	0.08
7-2A	0.65	0.11	3-3A	0.36	0.10
7-2B	0.52	0.13	3-3B	0.66	0.08

[1]see figure 1 for the tensiometer locations;
[2]arranged from the ridge to the upper weir;
[3]modeling efficiency;
[4]mean absolute bias

The mean and median *EF* values (not reported in table 6) are negative for the CB1 piezometers in all three sprinkling experiments. One factor that has a large effect on the *EF* values is the small range in observed pressure heads in the soil piezometers, relative to the larger range in pressure heads observed in tensiometers. Having a small range in an observed hydrologic-response observation causes the mean to be a good predictor of the observed value, relative to the *InHM* simulated value. The piezometer results in table 6 (along with the tensiometer results from table 4) show that the *MAB* is a more robust statistic for evaluating pressure head response at CB1, compared to the *EF*.

Soil-water content.— Figures 11A through 11D present time series of observed and simulated soil-water contents during sprinkling experiment 3. The observed and simulated soil-water contents are color coded by waveguide length in figures 11A and 11C, respectively. The observed and simulated soil-water contents are color coded by

TABLE 6

Model performance for observed versus InHM simulated pressure heads from the CB1 soil/saprolite and bedrock piezometers[1]

Experiment number	S / B[4]	Automated piezometers[2]			Manual piezometers[3]		
		Number of instruments[5]	Simulated saturation[6]	MAB[7]	Number of instruments	Simulated saturation	MAB
1	S	12	8	0.07	12	4	0.06
2	S	12	11	0.10	19	6	0.09
3	S	12	6	0.08	26	3	0.07
3	B	7	6	0.31	-	-	-

[1]see figure 1 for the piezometer locations
[2]piezometers with automated pressure transducers
[3]piezometers read manually
[4]soil/saprolite or bedrock piezometers
[5]the number of instruments is the number of responding piezometers for each experiment
[6]the number of observed responding piezometers that exhibited a simulated response
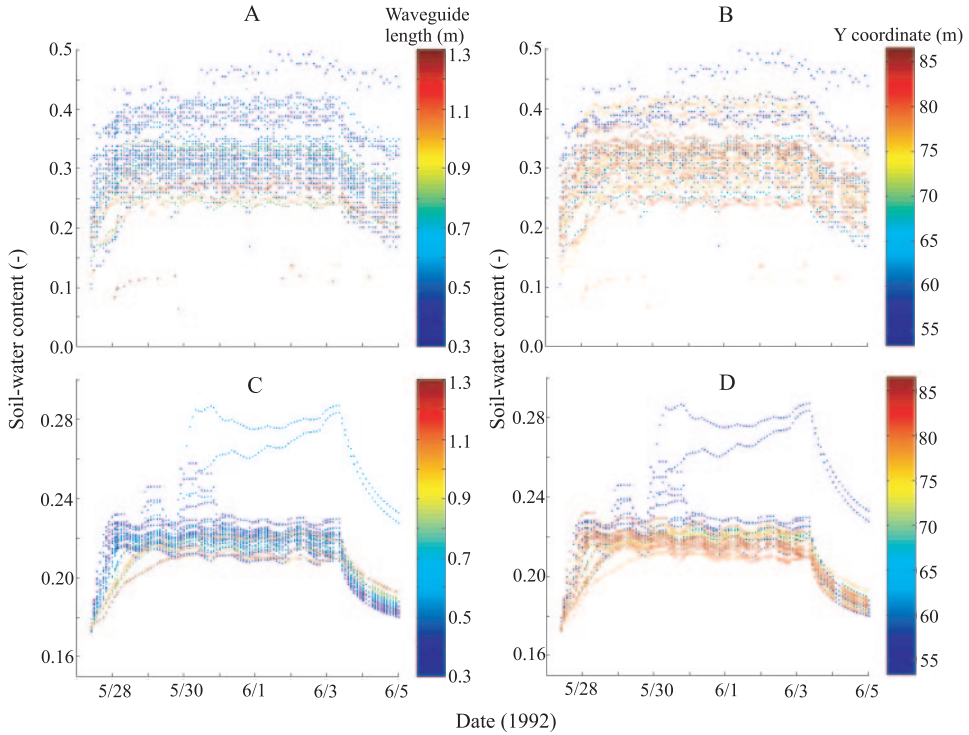[7]mean absolute bias

Fig. 11. Scatter plot of soil-water content time series for sprinkling experiment 3. (A) Observed soil-water content color coded by waveguide length. (B) Observed soil-water content color coded by Y coordinate (increasing upslope from the upper weir). (C) Simulated soil-water content color coded by waveguide length. (D) Simulated soil-water content color coded by Y coordinate (increasing upslope from the upper weir).

the Y coordinate, which increases moving upslope of the upper weir, in figures 11B and 11D. Comparison of the soil-water content time series in figures 11A through 11D indicates that the simulated water contents are underpredicted relative to the observed. During the quasi-steady period from 5/29/92 at midnight to 6/3 at 8am, the mean observed soil-water content (from all the TDR waveguides) was 0.32 m^3 m^{-3} and the simulated soil-water content was 0.22 m^3 m^{-3}. Based on only the soil-water content data, it could be concluded that *InHM* poorly simulated the CB1 soil-water contents. However, examination of the extremely steep wetting retention curve in figure 5A reveals that very small increases in pressure head result in large increases in soil-water content at slightly negative pressure heads near zero. The observed mean pressure head during the quasi-steady period of sprinkling experiment 3 was -0.051 m and the mean simulated pressure head was -0.095 m. Using the van Genuchten (1980) functional relationship to convert from the mean observed and simulated pressure heads to soil-water contents (based upon the wetting curve in fig. 5A) provides estimates for the observed quasi-steady soil-water content of 0.29 m^3 m^{-3} and for the simulated water content of 0.21 m^3 m^{-3}, suggesting that the inaccuracies in the *InHM* simulated soil-water contents occur because of undepredicting pressure heads rather than inaccuracies in the soil-water retention curves.

The observed temporal and spatial patterns shown in figures 11A and 11B are adequately reproduced in the simulated soil-water contents in figures 11C and 11D. For example, the deepest waveguides represented by the red (1.3 m), orange (1.05 m),

and green (0.8 m) scatter points in figures 11A and 11C consistently plot as the smallest observed and simulated soil-water contents. Shallower TDR waveguides represented by the dark blue (0.3 m) and light blue (0.55 m) scatter points in figures 11A and 11C are consistently larger for both the simulated and observed. When soil contents are color coded by the Y coordinate, there is a clear separation at 0.34 m^3 m^{-3} in figure 11B related to position in the CB1 catchment. The observed soil-water contents plotting above this line are all in the downgradient section of CB1 near the upper weir (the dark blue scatter points), with the exception of the three light orange scatter point time series at TDR waveguides located near platform 7 (see Ebel and others, 2007 for the platform locations). Simulated water contents in figure 11D match the observed pattern in figure 11B, with the dark blue scatter points plotting as higher simulated soil-water contents. Observed and simulated soil-water contents closer to the ridgecrest (the dark red and orange scatter points in figs. 11B and 11D) have lower observed and simulated values. Two time series of higher observed soil-water contents (above 0.45 m^3 m^{-3}) are visible in figure 11A, correspond to the same TDR waveguides with outlying high soil-water content time series in figures 11C and 11D. The diurnal fluctuations observed in the soil-water contents in figures 11A and 11B are also observed in figures 11C and 11D.

Saturation and pore pressure.—Beyond comparing only individual sets of observations, it is also important to evaluate the simulated distributed hydrologic response by combining the different observed data sets to examine saturation and pore-water pressure development in the CB1 subsurface (see Ebel and others, 2007). Figures 12A through 12F examine the observed and simulated soil saturation during the three sprinkling experiments. Figures 12A through 12C are the same saturation maps shown in the companion paper (Ebel and others, 2007). The observed saturation maps combine tensiometer and piezometer records and represent saturation that occurred at any time (rather than a snapshot in time) during the respective sprinkling experiment within the soil column (that is, fig. 12 does not indicate surface saturation). Figures 12D through 12F represent saturation development at the simulated observation points (the same observation points from figs. 12A though 12C) for the three sprinkling experiments. Comparison of the observed and simulated saturation through the soil column indicates that *InHM* simulates saturation very well in the bottom third of CB1, reasonably well in the middle third of CB1 and not as well in the top third of CB1. Some areas of patchy simulated saturation in figures 12D, 12E, and 12F correspond to localized regions of heavy sprinkling (see Ebel and others, 2007), where the saturation occurs in near-surface tensiometers, and small depressions in the soil-saprolite interface topography (in areas of thin saprolite), where the saturation occurs near the soil-saprolite interface.

Figures 13A through 13F present the observed and simulated pore-water pressure snapshots at the CB1 soil-saprolite interface (see the depth range in table 2) for the three sprinkling experiments at the times of peak observed pore-water pressure. Comparison of the observed and simulated pore-water pressures shows that both the simulated and observed pore water pressures are highest for experiment 2 and smallest for experiment 1. The area of higher pore pressure along the hollow axis is simulated by *InHM* for all three experiments, although the extent and magnitude of high pore-water pressure is underpredicted by *InHM* for experiments 1 and 3. The overlay of the 0.10 m saprolite thickness contour in figure 13F shows the role of the saprolite in draining the upper portions of CB1 in the simulations for all three simulated experiments. Examination of the observed pore-water pressures in figures 13A through 13C indicates that the spatial pattern of the saprolite draining effect is correctly simulated, although the simulated pore pressures in the upgradient areas of CB1 are less than the observed pore-water pressures. It is worth repeating that the interpolated
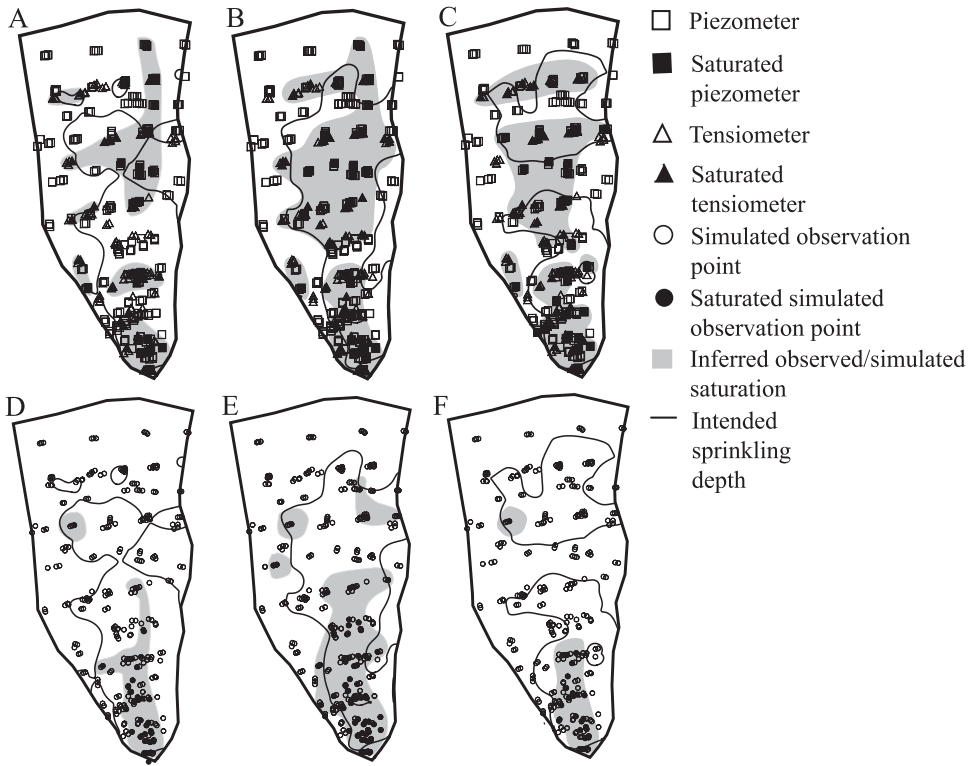
Fig. 12. Observed and simulated soil saturation during the three sprinkling experiments. (A) Observed saturation in tensiometers and piezometers during sprinkling experiment 1. (B) Observed saturation in tensiometers and piezometers during sprinkling experiment 2. (C) Observed saturation in tensiometers and piezometers during sprinkling experiment 3. (D) Simulated saturation during sprinkling experiment 1. (E) Simulated saturation during sprinkling experiment 2. (F) Simulated saturation during sprinkling experiment 3.

observed pore-water pressure snapshots are more qualitative than quantitative (see Ebel and others, 2007) and do not facilitate an exact quantitative comparison because of limitations in the methods used to create figures 13A, 13B, and 13C.

Further evaluation and analysis of the simulated pore-water pressures is provided by the detailed vertical cross sections through the CB1 soil during sprinkling experiment 3 at the time of peak observed pore-water pressures shown in figures 14 through 16. Figure 14 shows the locations of the vertical pore-water pressure cross-sections presented in figures 15 and 16. Figure 15 shows vertical slices of pore-water pressures at 20, 40, 60 and 80 percent of the distance between the upper weir and the ridge crest. Simulated pore-water pressures in figure 15 are relatively uniform and slightly below zero throughout CB1, except near the soil-saprolite interface. Cross sections C-C′ and D-D′ in figure 15 show that pore-water pressure in the soil increases slightly with depth and reaches a maximum at the soil-saprolite interface in the downgradient half of CB1, with elevated pore-water pressures along the hollow axis. Cross sections A-A′ and B-B′ in figure 15 also show elevated pore-water pressures along the hollow axis but are different from C-C′ and D-D′ in that areas of lower pressure occur near the soil-saprolite interface where saprolite is thicker (see fig. 13F).

Figure 16 presents a vertical slice of pore-water pressures passing through the upper weir, which is nearly along the surface topography hollow axis. Pore-water
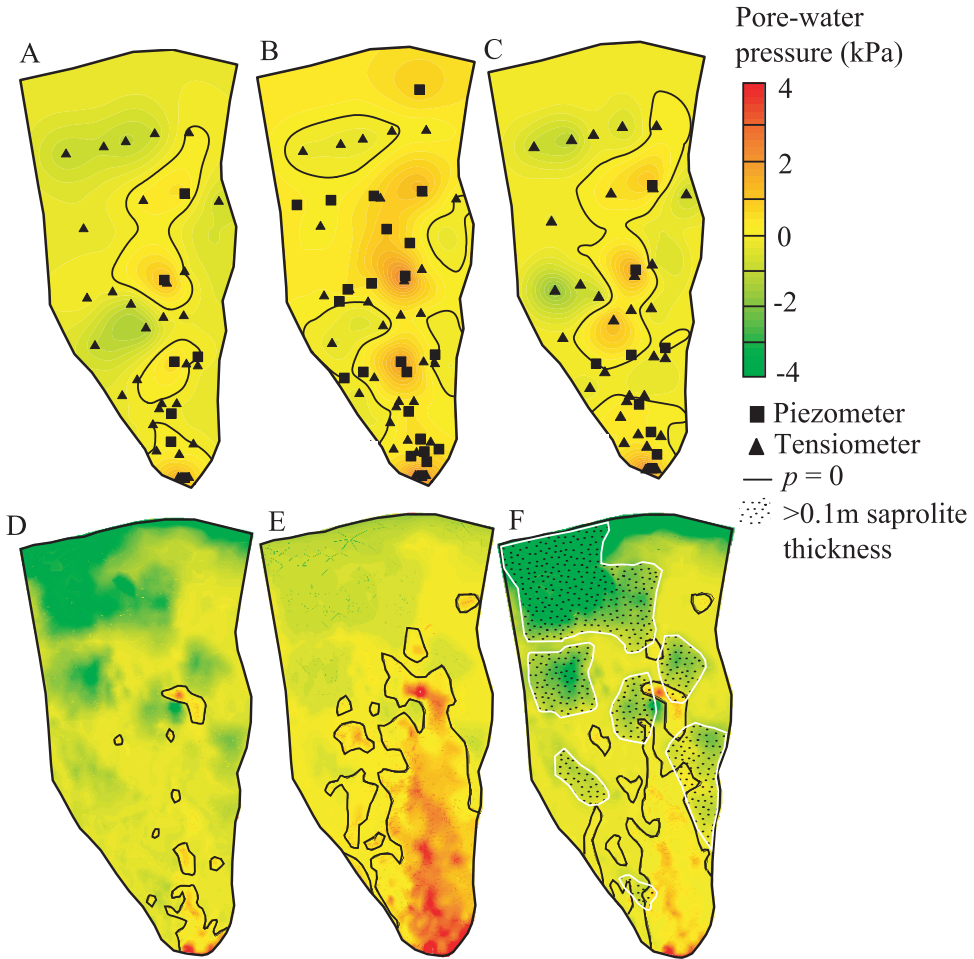
Fig. 13. Observed interpolated peak pore-water pressures from tensiometers and piezometers closest to the soil-saprolite interface and simulated pore pressures at the soil-saprolite interface. (A) Observed, sprinkling experiment 1 at 5/13/1990, 10:00 PM. (B) Observed, sprinkling experiment 2 at 5/27/1990, 9:00 AM. (C) Observed, sprinkling experiment 3 at 5/31/1992, 10:00 AM. (D) Simulated, sprinkling experiment 1 at 5/13/1990, 10:00 PM. (E) Simulated, sprinkling experiment 2 at 5/27/1990, 9:00 AM. (F) Simulated, sprinkling experiment 3 at 5/31/1992, 10:00 AM. The 0.1 m contour of saprolite thickness illustrates the role of the saprolite in draining the overlying colluvial soil.

pressure generally increases with depth, with the exception of areas drained by thick saprolite near the ridge crest in cross section E to F and F to G in figure 16. The role of soil-saprolite interface topography in generating pore-water pressure is illustrated by figure 16 by the higher pore-water pressure regions at depressions in the soil-saprolite interface in cross sections G to H, I to J, and to a lesser extent H to I. High pore-water pressures simulated at the downgradient BC near J are a result of the impermeable boundary at the upper weir (see fig. 3).

   Deuterium concentrations in lysimeters.—Table 7 presents the simulated and observed deuterium concentrations in the responding CB1 lysimeters during sprinkling experiment 3. The first number identifying the lysimeters in table 7 is the platform number (see Ebel and others, 2007 for the platform locations). For example, lysimeter 9-3 is the
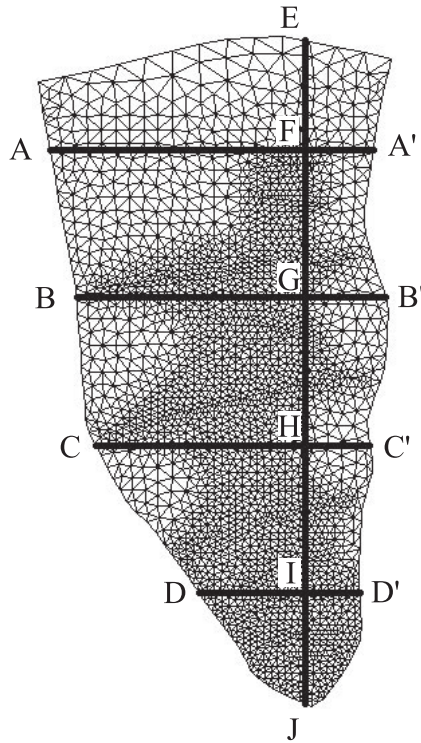
Fig. 14. Diagram showing the locations of the pore-water pressure cross sections illustrated in figures 15 and 16 overlain on a plan view of the CB1 finite-element mesh.

third lysimeter located along platform nine. Responding lysimeters are defined as lysimeters reaching $\delta D\text{‰}$ values greater than zero. Nine of the eleven observed responding lysimeters exhibit a simulated response. The simulated $\delta D\text{‰}$ values in table 7 are less than the observed $\delta D\text{‰}$, with the exception of lysimeters 9-1, 9-2, and 9-3. The timing of peak concentrations in the CB1 lysimeters was well simulated by *InHM*, as shown by the small percent differences in table 7. In most lysimeters, the peak concentration arrival is simulated slightly before the observed arrival. It is worth noting that a second solute transport simulation with almost no dispersion (longitudinal dispersitivity equal to 0.01 m and the two transverse dispersivities equal to 0.001 m) was also conducted for sprinkling experiment 3. The case of near-zero dispersion had a sharper concentration profile with higher peak concentrations but a more delayed timing of peak concentration, relative to the observed. It is likely that with calibration of the susburface dispersivities for CB1 (for example, between the values used in this study and zero) that the δD peak concentrations and arrival times could be simulated better than the values reported in table 7.

DISCUSSION

Problems, Limitations, and Sensitivity Analyses

 Problems with soil-hydraulic parameters.—Based on evaluation of observed versus simulated hydrologic response from figures 6 though 16 and tables 3 through 7, *InHM* successfully simulated the integrated and distributed hydrologic response at the CB1 catchment. However, it is also clear from examination of figures 6 through 16 and
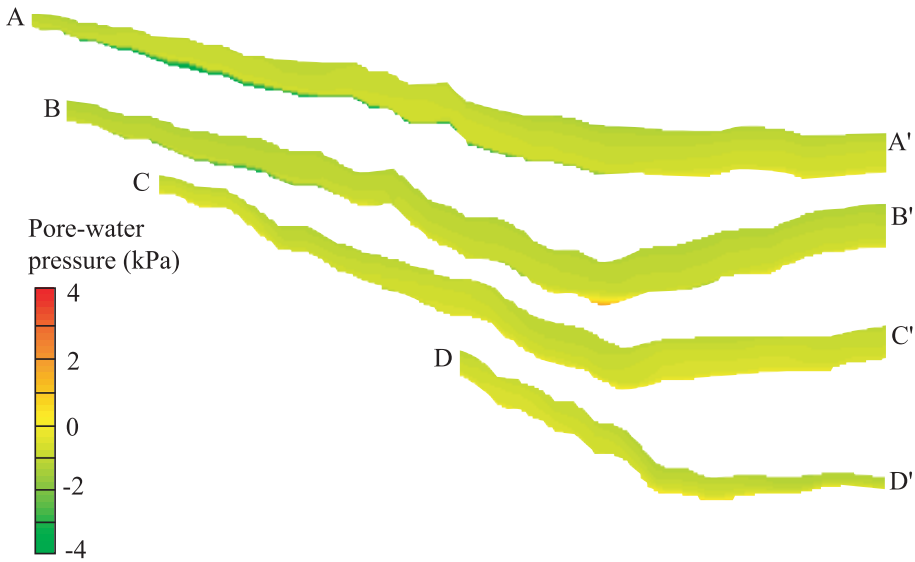
Fig. 15. Vertical cross sections of pore-water pressure in the CB1 soil, see figure 14 for cross section locations.

tables 3 through 7 that the simulated hydrologic response is not a perfect match to the observed data. One of the largest problems with the *InHM* simulations reported in this paper is the fracture flow component of hydrologic response. Piezometric response and tracer studies at CB1 indicated that shallow bedrock fracture flow played a large role in runoff and pore-water pressure generation (Montgomery and others, 1997, 2002; Anderson and others, 1997a). The CB1 lower weir was designed to capture the bedrock flow component of runoff. Figure 17 shows the simulated and observed lower weir hydrograph and mean sprinkling rate hyetograph. The simulated lower weir discharge underpredicts the observed lower weir discharge by nearly a factor of four. In this study, the weathered bedrock saturated hydraulic conductivity was set to be the same as the unweathered bedrock because of the large variation (4 orders of magnitude) in slug-test estimated saturated hydraulic conductivities in the CB1 weathered bedrock. Without knowledge of the spatial distribution of fractures, fracture apertures, and fracture connectivity it is difficult to estimate either the volume fractions of fractures necessary to utilize a dual continuum approach or spatially variable effective conductivities. Obviously, mischaracterizing the effective bedrock saturated hydraulic conductivity could result in underpredicting the lower weir discharge. It should be pointed out that the water that does not leave CB1 through the upper weir and cannot be accounted for at the lower weir goes to storage in the unweathered bedrock and out the local head boundary (EHJI in fig. 3).

While the integrated hydrologic-response at the lower weir (that is, the discharge) illustrates the effect of not representing the component of hydrologic-response driven by fracture flow, the distributed response reveals the spatially-variable nuances. For example, Montgomery and others (1997, 2002) concluded that fracture flow from the weathered bedrock at CB1 controls the locations of pore-water pressure hotspots. The interpolated observed pore-water pressure hotspots in figures 13A, 13B, and 13C in the lower half of CB1 (see Montgomery and others, 2002) are in the area of the bedrock fracture locations mapped after the 1996 CB1 landslide (see Montgomery and others, in preparation).These hotspots are not reproduced in figures 13D, 13E, and 13F
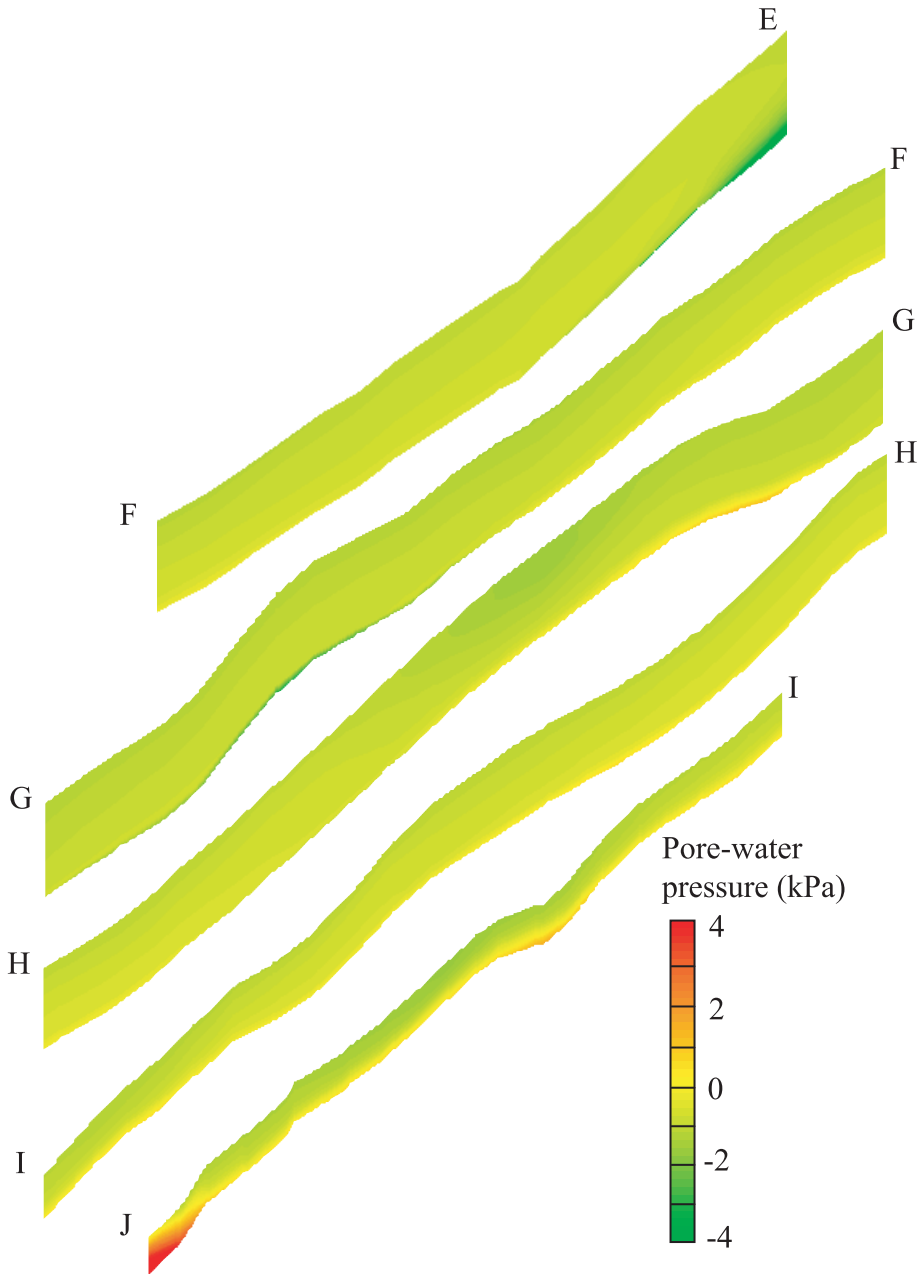
Fig. 16. Vertical cross section of pore-water pressure in the CB1 soil along the long-axis of the catchment. See figure 14 for the cross section location.

because information on fracture apertures, densities, and connectivity for CB1 is unavailable, precluding simulation of these small-scale pore-water pressure hotspots.

The retention curves of the saprolite, weathered bedrock, and bedrock were unmeasured at the site and taken from literature values. Calculations using the

Table 7

Observed and InHM simulated peak and time to peak for deuterium concentrations at the responding CB1 lysimeters[1,2]

Experiment Number	Lysimeter[2]	Peak concentration (δD‰)			Time to peak concentration (days)[3]		
		Observed	Simulated	Percent difference	Observed	Simulated	Percent difference
3	2-1C	58.3	-18.9	132.4	8.1	11.9	-47.4
3	5-2	118.5	4.8	95.9	6.9	5.9	14.2
3	5-8	166.4	2.1	98.8	6.0	6.0	0.2
3	6-2	93.5	3.8	95.9	6.0	6.0	0.1
3	6-4	85.4	-0.7	100.9	7.3	6.1	16.5
3	6-5	107.4	0.6	99.4	6.9	6.0	13.1
3	9-1	-24.7	6.7	127.0	6.92	6.0	12.9
3	9-2	-24.1	3.3	113.7	6.0	6.1	-0.9
3	9-3	1.1	10.9	-893.1	6.9	6.0	13.1
3	9-5	53.0	8.5	83.9	6.9	6.0	13.1
3	9-8	101.4	2.0	98.1	6.9	5.9	14.2

[1]see figure 1 for the lysimeter locations, also note that the lysimeters are identified by platform number (see Ebel and others, 2007) followed by an instrument number
[2]responding lysimeters exhibit maximum δD‰ greater than 0;
[3]time to peak (observed/simulated) minus the start time for the observed runoff event

hydraulic conductivity functions of the soil (wetting retention curve) and saprolite indicates that until the pressure head in the soil exceeds -0.05 m pressure head, the saprolite unsaturated hydraulic conductivity is greater than the soil unsaturated hydraulic conductivity because the saturated hydraulic conductivity of the two layers does not differ by much (see table 2). This explains why the upgradient sections of CB1 are drained so effectively by the thicker saprolite in that region of the catchment and offers an explanation as to why soil saturation (fig. 12) and pore-water pressure (figs. 13, 15, and 16) are not simulated as well in the upgradient portion of CB1 as in the downgradient portion. Clearly, the soil-hydraulic properties of the saprolite and weathered bedrock are important for simulating the CB1 hydrologic response accurately and with better hydraulic parameter estimates for these hydrogeologic layers, the simulation results reported herein would likely improve.

Another limitation on the ability of the *InHM* simulations reported here is the use of spatially homogeneous soil hydraulic parameters within each hydrogeologic layer (see fig. 4). Previous analysis of CB1 soil-hydraulic parameter estimates demonstrated spatial variability in saturated hydraulic conductivity (Montgomery and others, 1997, 2002), porosity (Torres and others, 1998; Schmidt, ms, 1999), and soil characteristic curves (Torres and others, 1998). It is to be expected that omitting the spatial variability in soil hydraulic parameters will negatively affect the distributed simulation results. Perusal of figures 8A and 8C reveals considerable scatter in the IC pressure heads that likely reflects heterogeneity in soil-water retention curves, porosity, and saturated hydraulic conductivity that are not represented with the CB1 parameterization used in this study. Montgomery and Dietrich (2002) determined that ICs of soil moisture and vadose zone characteristics strongly influence the timing of runoff generation at CB1. Without the soil hetereogeneity that facilitates accurate simulation of ICs, it should be expected that there are limitations to how well models like *InHM* can simulate event-based hydrologic response. Soil porosity (Schmidt, ms, 1999) and saturated hydraulic conductivity (Montgomery and others, 2002; Ebel and others,
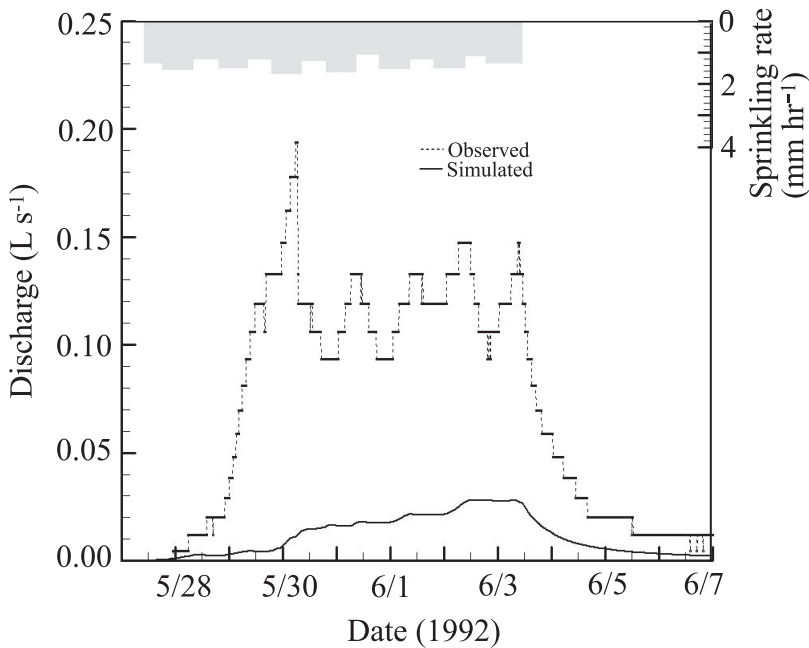
Fig. 17. Observed and simulated discharge hydrograph at the CB1 lower weir and mean sprinkling rate hyetograph for sprinkling experiment 3.

2007) were also observed to decline with depth, albeit not consistently enough to allow an estimation of those parameters that could be employed in the CB1 boundary-value problem used here. Anisotropy of the saturated porous media at CB1 was not considered in this study because no information on directional saturated hydraulic conductivities was available.

Additional parameterization problems that affect the simulated CB1 hydrologic response reported here include the errors associated with representing porous media that includes preferential flowpaths using effective hydraulic parameters (see, for example, Binley and others, 1989; Yeh and Harvey, 1990; Kitanidis, 1990; and Eaton and McCord, 1995). CB1 has macropores in the form of Mountain beaver (*Aplodontia rufa)* burrows ~0.2 m in diameter and to depths of 1.2 – 2.0 m extending up to 100 m in length with openings every 6 – 7 m (Schmidt, ms, 1999). The tracer experiments of Anderson and others (1997a) do not indicate preferential flow through soil macropores during the third sprinkling experiment. The hydrologic threshold for preferential flow through the soil macropores at CB1 is not known. Near surface bedrock fractures function as preferential flow paths (Montgomery, ms, 1991). While *InHM* is capable of representing preferential flowpaths using a Darcian dual-continuum approach, employing that approach at CB1 to represent macropores and fractures would be nothing more than a calibration exercise, which was not the goal of this research effort.

Effect of hysteresis.—To examine the effect of hysteresis, a hydrologic-response simulation was conducted for CB1 sprinkling experiment 3 using the wetting soil-water retention curve shown in figure 5A with no hysteretic flow. Figure 18 shows the observed, base-case simulated, and non-hysteretic simulated total head time series for tensiometer nest 5 – 4 (as shown in fig. 10E). Figure 18 provides a basis to generalize
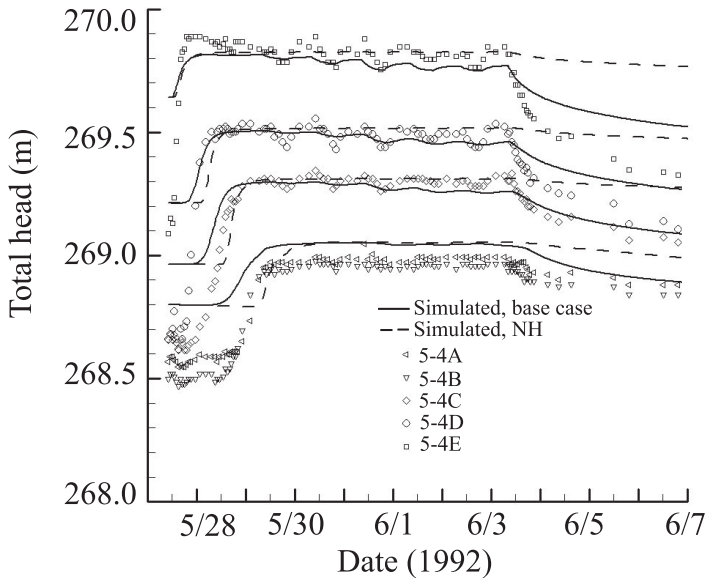
Fig. 18. Simulated tensiometer total head time series with no hysteresis (NH) for tensiometer nest 5-4 employing the wetting soil-water retention curve from figure 5A.

the effects of hysteresis on the unsaturated zone hydrologic response simulation at CB1. The rising limb of tensiometric response is always slower for the non-hysteretic case relative to the base case because hysteretic wetting occurs on a scanning curve from the main drying curve with higher saturation, and therefore higher hydraulic conductivity, for a given pressure head. The largest difference between the base case and the non-hysteretic simulated total head time series is the drying limb, where the base case provides a much better representation of the drying behavior of the unsaturated zone at CB1. Neglecting hysteresis results in poor simulated hydrologic response during drainage at CB1, which is consistent with studies at other locations (for example, Si and Kachanowski, 2000). The diurnal pressure head fluctuations in figure 10 are also not simulated well without hysteresis (see fig. 18).

The simulated tensiometer time series in figure 18 also illustrates the slight continuous decline in the base-case simulated pressure heads. This continuous decline in pressure head over time is an artifact of the method used to represent hysteretic scanning curves in the *InHM* simulations, which causes "pumping" for repeated wetting and drying if the pressure head changes are not sufficient to close the scanning curves onto the main hysteresis loops (Jaynes, 1990). Although problems exist with simulated pressure heads (on the order of a few centimeters) because of pumping effects, it is clear from figure 18 that incorporating hysteresis is important at CB1 for simulating distributed hydrologic response, particularly for drying conditions. It is worth noting that a decrease in simulated pressure head of only a few centimeters at near-zero pressure heads, as a result of pumping, could explain part of errors in simulated water content in figures 11C and 11D.

Boundary conditions.—One limitation of the simulations reported here was the limited temporal resolution of the sprinkling intensity data applied as the surface BC. Ebel and others (2007) and Anderson and others (1997a) demonstrated the effect of spatially variable sprinkling intensities on observed hydrologic response. While the

simulated hydrologic response reflects some of the diurnal fluctuations related to sprinkling variability, it is clear that this capability would be improved by more detailed temporal resolution in the sprinkling intensities than is provided by the twice daily manual rain gage readings (see Ebel and others, 2007). To examine whether this problem could be remedied by using the automated rain gages that have 10 minute temporal resolution, a hydrologic-response simulation was conducted for sprinkling experiment 2 using the mean sprinkling rate recorded in the three automated rain gages at CB1 as the surface BC. The automated rain gage simulated hydrograph drastically underpredicts the upper weir discharge (not shown), largely because the automated rain is on average 30 percent less than what was recorded in the nearest manual rain gage. The automated rain gage errors occur because of undercatch associated with the fine spray from the sprinklers (see Ebel and others, 2007) and the elevated heights of the automated rain gages (Torres, ms, 1997). Because of the problems with the automated rain gages during the sprinkling experiments, the limited temporal resolution of the manual rain gage observations is an unresolvable problem.

Another BC difficulty is associated with the representation of the downgradient BC at the upper weir. For example, the three tensiometers near the upper weir are too close to the downgradient BC and exhibit elevated pore-water pressures in figures 8A, 8B, and 8C (the pressure heads that corkscrew upward near 0.5 m simulated pressure head). Furthermore, greater than half the simulated tensiometers with negative *EF* values for experiments 1 and 3 were in row 3 or below, illustrating the difficulties with representing the CB1 upper weir in *InHM*.

The sensitivity of *InHM* simulation results to the deeper subsurface downgradient BC (that is, the local head BC) was examined by simulating the experiment 3 hydrologic response using a radiation BC that employs a back calculated gradient to determine the boundary flux rather than equation (7). The tensiometer *MAB* differed by only 0.001 m between the base case with the local head downgradient BC and the radiation BC. The simulated radiation BC discharge had exactly the same time to peak discharge as the base case, but with a slightly higher peak discharge of $0.128 \, \mathrm{Ls^{-1}}$ and an *EF* of 0.64. Based on these results, the CB1 upper weir discharge is only slightly sensitive to the deeper downgradient BC while the vadose zone hydrologic response is insensitive to the downgradient BC. Combining the insensitivity of the simulated vadose zone response to the deeper downgradient BC and the poorer simulated tensiometric response near the upper weir suggests that there are inaccuracies in the representation of the impermeable BC specified at the CB1 upper weir.

To examine the effect of an impermeable BC at the weathered bedrock-saprolite boundary, another hydrologic-response simulation was conducted for experiment 3. An impermeable boundary was mimicked by setting the saturated hydraulic conductivity of the weathered bedrock and bedrock layers to $1 \times 10^{-13} \, \mathrm{m \, s^{-1}}$, a value that is essentially impermeable. The simulated runoff coefficients for the impermeable case is 0.87, compared to the base case simulated runoff coefficient of 0.29 and the observed runoff coefficient of 0.34, calculated using the integrated kriged sprinkling volume from Ebel and others (2007). Simulated pore-water pressures (not shown) were also oversimulated relative to the observed because having an impermeable basal BC does not allow the infiltrating water to enter the bedrock flow system.

Literature parameters.—Hydrologic modeling studies frequently employ soil-hydraulic parameters that are based on soil textural analysis or minimal site measurements. To investigate the effect of detailed site characterization, a hydrologic-response simulation was conducted for sprinkling experiment 3 that employed the soil-hydraulic parameters previously reported for the CB1 site. Table 8 summarizes the soil-hydraulic parameters used for this simulation. All the hydrogeologic layer geom-

TABLE 8

Hydrogeologic properties of the CB1 boundary-value problem taken from previous publications

Layer [1]	Thickness (m)	Porosity ($m^3\ m^{-3}$)	Saturated hydraulic conductivity ($m\ s^{-1}$)	Compressibiliy (ms^2kg^{-1})
Soil	0.04 - 1.5 [2]	0.71 [4]	1.0×10^{-4} [6]	1×10^{-8} [7]
Saprolite	0.02 - 1.1 [2]	0.15 [5]	4.7×10^{-5} [6]	1×10^{-9} [7]
Weathered bedrock	0.02 - 4.0 [3]	0.15 [5]	4.7×10^{-5} [6]	1×10^{-9} [7]
Bedrock	50	0.12 [5]	5.0×10^{-7}	1×10^{-9} [7]

[1]see figure 4;
[2]Kriged from 630 data points (Schmidt, ms, 1999), including the CB1 piezometer installation
[3]from Anderson (ms, 1995);
[4]Anderson and others (1997b)
[5]estimated from figure 3 in Anderson and others (2002)
[6]Montgomery and others (2002);
[7]Freeze and Cherry (1979)

etries are the same as in figure 4 and the BC are the same except that the sprinkling rate used for the surface BC is the intended sprinkling rate of 1.65 mm h^{-1} (see Ebel and other, 2007). The largest differences between the base-case simulation and the literature parameter (LP) simulation described in table 8 are the soil porosity and the soil retention curve, which is based on soil-textural analysis (see Torres and others, 1998) and the van Genuchten parameters reported by Carsel and Parrish (1988) for a sandy loam (that is, α equal to 7.5 m^{-1} and n equal to 1.89). It is worth noting that the ICs were re-estimated employing the soil-hydraulic parameters in table 8 to accurately portray the effect of the changed parameterization. Hysteresis was not included in the LP simulation because the soil-water retention curve from Torres and others (1998), based on soil textural analysis, was for wetting only.

Figure 19 presents the observed, base-case simulated, and LP simulated upper weir discharge along with the sprinkling rate hyetographs (the solid black line hyetograph is the LP sprinkling rate). The initial discharge at the CB1 upper weir is too large relative to the observed, because the soil is still draining following the sprinkling tests that occurred prior to experiment 3. Comparison of the receding limb of the LP simulated hydrograph also lags well behind the base-case simulated and observed hydrographs, which is likely the result of a smaller saturated hydraulic conductivity for the soil, a larger soil porosity, and less steep characteristic curves for the soil. The peak LP discharge is larger than the base-case simulated and observed peak discharges because the sprinkling rates are higher for the LP case (see Ebel and others, 2007 for a discussion of the CB1 sprinkling water balance).

Figure 20 shows the observed, base-case simulated, and LP simulated total head time series for tensiometer nest 5 – 4. The LP simulated time series of total head are dashed lines and are labeled with the corresponding observed tensiometer. Examination of figure 20 demonstrates that the LP simulation poorly represents the observed total heads in the CB1 subsurface. Only 20 out of 101 tensiometers had positive *EF* values for pressure heads (compared to 73 for the base case) and the *MAB* for the LP simulated tensiometers was 0.32 m (compared to 0.13 m for the base case). The soil-hydraulic parameter having the largest effect on *InHM* simulated hydrologic response at CB1 is the soil-water retention curves. The evidence presented here indicates that soil-water retention curves based on textural analysis are inadequate (as suggested by Beven, 1989) when compared to those derived from careful field
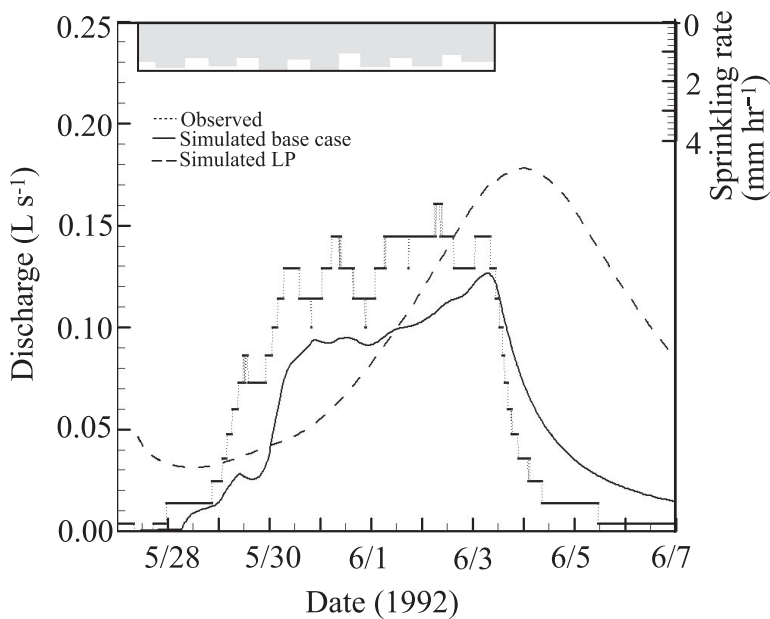
Fig. 19. Observed, base-case simulated, and literature-parameter (LP) simulated CB1 upper weir discharge hydrographs and sprinkling rate hyetograph for sprinkling experiment 3.

measurements like those of Torres and others (1998). One potential reason why the *in-situ* measurements outperform the estimates based on soil-textural classifications is that the *in-situ* retention curve estimates may implicitly include the effects of preferential flow paths.

<div align="center">SUMMARY</div>

In the spirit of Robert E. Horton's measure and model protocol, the effort reported herein combines the unrivaled CB1 data set and the comprehensive physics-based *InHM,* facilitating rigorous hydrologic-response simulation for three catchment-scale sprinkling experiments. The importance of synthesizing integrated and distributed hydrologic-response observations for parameterization and evaluation of physics-based models is demonstrated. Runoff generation at the upper weir, tensiometric/piezometric response in the soil, pore-water pressure generation at the soil-saprolite interface, and solute (tracer) transport at the upper weir and at lysimeters were all well simulated in this study with *InHM.* Cross sections of peak pore-water pressure during sprinkling experiment 3 indicate that the 3D soil-saprolite-weathered bedrock interface topography can affect the spatial distribution to pore-water pressure hotspots. Maps of simulated pore-water pressure and saturation development indicate that thick saprolite can drain the overlying soil, preventing the development of soil saturation and pore-water pressure. The results presented herein show that detailed characterization of saprolite and weathered bedrock thickness and hydraulic properties, as suggested by Montgomery and others (2002), is critical for simulating pore-water pressure generation at sites like CB1 where convergent subsurface flow and fracture flow is important.

While the CB1 data set provided an excellent test of the *InHM* hydrologic-response simulation capability, important information related to parameterizing the
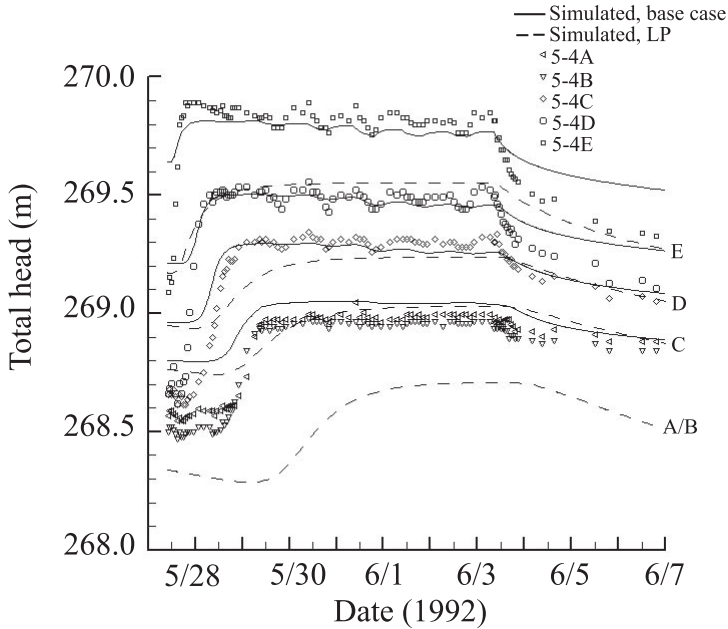
Fig. 20. Observed, base-case simulated, and literature parameter (LP) simulated total head time series from tensiometer nest 5-4 during sprinkling experiment 3. The LP time series are labeled with the letter of the corresponding tensiometer.

weathered bedrock and bedrock layers at CB1 was missing. The inability to accurately estimate the geometry and hydraulic properties of the layered hydrogeologic units at CB1 for this study prevented detailed simulation-based assessment of the weathered bedrock piezometric response and runoff generation at the lower weir, which are primarily controlled by fracture flow. Without the detailed field measurements at CB1, it is unlikely that the model component of the measure and model approach would have identified fractured bedrock flow as an important process. Sensitivity analyses demonstrate that hysteretic flow is important in the CB1 soil and that modeling layered geologic interfaces (such as the saprolite-weathered bedrock contact) with an impermeable BC leads to large inaccuracies in simulated magnitudes of runoff generation and pore-water pressure development. Comparison of hydrologic-response simulations using soil-water retention curves measured at CB1 (Torres and others, 1998) versus estimates based solely on soil-textural analysis shows that field-based measurements can dramatically improve variably-saturated hydrologic response simulation.

The hydrologic-response simulations reported herein identify some of the limitations of physics-based models like *InHM*. In particular, the large parameterization data requirements and difficulties with initial and boundary conditions are problematic. It is our opinion that models like *InHM* are currently best suited for concept development simulations of the type discussed by Weiler and McDonnell (2004). The conclusion of Stephenson and Freeze (1974) that an unprecedented and massive data collection campaign would be needed before comprehensive physics-based hydrologic-response models (see Freeze and Harlan, 1969) can be meaningfully employed at a regional-scale for operational hydrology is still valid today. However, the aforementioned limitations of physics-based models do not amount to a "death sentence" (see, for example, Savenije, 2001) for models like *InHM*. The rise of disciplines like hydrogeomorphology (for example, Sidle and Onda, 2004), hydroecology (for ex-

ample, Rodriguez-Iturbe and Porporato, 2004), and hydropedology (for example, Lin and others, 2006) has set the stage for heuristic hydrologic simulations that clarify the process linkages in complex hydrologically-driven systems that are 3D, transient, and variably-saturated. In addition to concept development, comprehensive physics-based hydrologic-response simulation has the potential for pushing the boundaries of hypothesis testing (for example, Cloke and others, 2006) and field experiment design (see Dunne, 1983; Klemes, 1986; Seibert and McDonnell, 2002, 2003) that is not possible with simpler models (see Loague and VanderKwaak, 2004; Loague and others, 2006; Ebel and Loague, 2006).

With regard to the role of multiple types of hydrologic response data reducing equifinality (see Ebel and Loague, 2006), uncertainties in initial and boundary conditions (see Stephenson and Freeze, 1974) make the complete elimination of equifinality for event-based simulations (like those conducted in this paper) unlikely, despite large numbers of distributed measurements for model evaluation. One promising approach for both reducing equifinality, relative to boundary and initial conditions, and providing a more robust test of models like InHM is continuous simulation of long-term hydrologic response. In continuous simulation, boundary conditions and model parameterizations that do not adequately characterize the true physical system will become more apparent as a larger range of hydrologic events (that is, storm depths, maximum rates, and durations) and conditions (prolonged wet and dry periods that impact initial conditions) are simulated and evaluated against distributed data sets.

REFERENCES

Ambroise, B., Beven, K. J., and Freer, J., 1996a, Toward a generalization of the TOPMODEL concepts: Topographic indices of hydrological similarity: Water Resources Research, v. 32, p. 2135–2145.
Ambroise, B., Freer, J., and Beven, K. J., 1996b, Application of a generalized TOPMODEL to the small Ringelback catchment, Vosges, France: Water Resources Research, v. 32, p. 2147–2159.
Anderson, M. G., and Burt, T. P., 1978, Toward more detailed field monitoring of variable source areas: Water Resources Research, v. 14, p. 1123–1131.
Anderson, S. P., ms, 1995, Flow paths, solute sources, weathering, and denudation rates: The chemical geomorphology of a small catchment: Berkeley, California, University of California, Berkeley, Ph. D. thesis, 380 p.
Anderson, S. P., Dietrich, W. E., Montgomery, D. R., Torres, R., Conrad, M. E., and Loague, K., 1997a, Subsurface flowpaths in a steep, unchanneled catchment: Water Resources Research, v. 33, p. 2637–2653.
Anderson, S. P., Dietrich, W. E., Torres, R., Montgomery, D. R., and Loague, K., 1997b, Concentration discharge relationships in runoff from a steep, unchanneled catchment: Water Resources Research, v. 33, p. 211–225.
Anderson, S. P., Dietrich, W. E., and Brimhall, G. H., 2002, Weathering profiles, mass-balance analysis, and rates of solute loss: Linkages between weathering and erosion in a small, steep catchment: GSA Bulletin, v. 114, p. 1143–1158.
Beven, K. J., 1977, Hillslope hydrographs by the finite element method: Earth Surface Processes, v. 2, p. 13–28.
———— 1978, The hydrological response of headwater and sideslope areas: Hydrological Sciences Bulletin, v. 23, p. 419–37.

—— 1989, Changing ideas in hydrology: the case of physically based models: Journal of Hydrology, v. 105, p. 157–172.

—— 1993, Prophesy, reality and uncertainty in distributed hydrological modeling: Advances in Water Resources, v. 16, p. 41–51.

—— 1997, TOPMODEL: a critique: Hydrological Processes, v. 11, p. 1069–1086.

—— 2000, Uniqueness of place and process representations in hydrological modeling: Hydrology and Earth Systems Sciences, v. 4, p. 203–213.

—— 2004, Robert E. Horton's perceptual model of infiltration processes: Hydrological Processes, v. 18, p. 3447–3460.

—— 2006, A manifesto for the equifinality thesis: Journal of Hydrology, v. 320, p. 18–36.

Binley, A. B., and Beven, K. J., 1992, Three-dimensional modeling of hillslope hydrology: Hydrological Processes, v. 6, p. 347–359.

Binley, A. B., Beven, K. J., and Elgy, J., 1989, A physically based model of heterogeneous hillslopes, 2, effective hydraulic conductivities: Water Resources Research, v. 25, p. 1228–1233.

Bronstert, A., and Plate, E. J., 1997, Modelling of runoff generation and soil moisture dynamics for hillslopes and micro-catchments: Journal of Hydrology, v. 198, p. 177–195.

Cappus, P., 1960, Bassin expérimental d'Alrance – étude des lois de l'écoulement – application au calcul et à la prévision des débits: La Houille Blanche, v. A, p. 493–520.

Carsel, R. F., and Parrish, R. S., 1988, Developing joint probability distributions of soil water retention characteristics: Water Resources Research, v. 24, p. 755–769.

Chow, V. T., 1959, Open-channel hydraulics: New York, McGraw-Hill Book Company, 680 p.

Cloke, H. L., Anderson, M. G., McDonnell, J. J., and Renaud, J. P., 2006, Using numerical modeling to evaluate the capillary fringe groundwater ridging hypothesis of streamflow generation: Journal of Hydrology, v. 316, p. 141–162.

Coles, N. A., Sivapalan, M., Larsen, J. E., Linnet, P. E., and Fahrner, C. K., 1997, Modelling runoff generation small agricultural catchments: can real world processes be captured?: Hydrological Processes, v. 11, p. 111–1136.

Dhakal, A. S., and Sidle, R. C., 2004, Pore water pressure assessment in a forest watershed: Simulations and distributed field measurements related to forest practices: Water Resources Research, v. 40, W02405, doi:10.1029/2003WR002017.

Dunne, T., 1983, Relation of field studies and modeling in the prediction of storm runoff: Journal of Hydrology, v. 65, p. 25–48.

Dunne, T., and Black, R. G., 1970a, An experimental investigation of runoff production in permeable soils: Water Resources Research, v. 6, p. 478–490.

—— 1970b, Partial area contributions to storm runoff in a small New England watershed: Water Resources Research, v. 6, p. 1296–1311.

Eaton, R. R., and McCord, J. T., 1995, Effective hydraulic conductivities in unsaturated heterogeneous media by Monte Carlo simulation: Transport in Porous Media, v. 18, p. 203–216.

Ebel, B. A., and Loague, K. M., 2006, Physics-Based Hydrologic Response Simulation: Seeing through the Fog of Equifinality: Hydrological Processes, v. 20, p. 2887–2900.

Ebel, B. A., Loague, K., Dietrich, W. E., Montgomery, D. R., Torres, R., Anderson, S. P., and Giambelluca, T. W., 2007, Near-surface hydrologic response for a steep, unchanneled catchment near Coos Bay, Oregon: 1. Sprinkling experiments: American Journal of Science, v. 307, p. 678–708.

Franks, S. W., Gineste, Ph., Beven, K. J., and Merot, Ph., 1998, On constraining the predictions of a distributed model: the incorporation of fuzzy estimates of saturated areas into the calibration process: Water Resources Research, v. 34, p. 787–797.

Freer, J. E., McMillan, H., McDonnell, J. J., and Beven, K. J., 2004, Constraining dynamic TOPMODEL responses for imprecise water table information using fuzzy rule based performance measures: Journal of Hydrology, v. 291, p. 254–277.

Freeze, R. A., 1971, Three-dimensional transient saturated-unsaturated flow in a groundwater basin: Water Resources Research, v. 7, p. 347–366.

—— 1972a, Role of subsurface flow in generating surface runoff: 1. Base flow contributions to channel flow: Water Resources Research, v. 8, p. 609–624.

—— 1972b, Role of subsurface flow in generating surface runoff: 2. Upstream source areas: Water Resources Research, v. 8, p. 1272–1283.

—— 1978, Mathematical models of hillslope hydrology, *in* Kirkby, M. J., editor, Hillslope Hydrology: New York, Wiley, p. 177–225.

Freeze, R. A., and Cherry, J. A., 1979, Groundwater: Englewood Cliffs, New Jersey, Prentice-Hall, 604 p.

Freeze, R. A., and Harlan, R. L., 1969, Blueprint for a physically-based digitally simulated, hydrologic response model: Journal of Hydrology, v. 9, p. 237–258.

Gelhar, L. W., 1993, Stochastic subsurface hydrology: Englewood Cliffs, New Jersey, Prentice-Hall, 390 p.

Grayson, R. B., Moore, I. D., and McMahon, T. A., 1992, Physically based hydrologic modeling, 1, A terrain based model for investigative purposes: Water Resources Research, v. 28, p. 2639–2658.

Grayson, R. B., Blöschl, G., and Moore, I. D., 1995, Distributed parameter hydrologic modeling using vector elevation data: THALES and TAPES-C, *in* Singh, V. P., editor, Computer models in watershed hydrology, Fort Collins, CO: Highlands Ranch, Colorado, Water Resources Publications, chapter 19, p. 669–696.

Grayson, R B, Blöschl, G., Western, A. W., and McMahon, T. A., 2002, Advances in the use of observed spatial patterns of catchment hydrological response: Advances in Water Resources, v. 25, p. 1313–1334.

Heppner, C. S., Loague, K., and VanderKwaak, J. E., 2007, Long-term InHM Simulations of hydrologic response and sediment transport for the R-5 catchment: Earth Surface Processes and Landforms, doi:10.1002/esp.1474.

Iverson, R. M., Reid, M. E., Iverson, N. R., LaHusen, R. G., Logan, M., Mann, J. E., and Brien, D. L., 2000, Acute sensitivity of landslide rates to initial soil porosity: Science, v. 290, p. 513–516.

Jackson, C. R., and Cundy, T. W., 1992, A model of transient, topographically driven, saturated subsurface flow: Water Resources Research, v. 28, p. 1417–1427.

James, L. D., and Burges, S. J., 1982. Selection, calibration and testing of hydrologic models, *in* Haan, C. T., Johnson, H. P., and Brakensiek, D. L., editors, Hydrologic Modeling of Small Watersheds: St. Joseph, Michigan, American Society of Agricultural Engineers, p. 437–472.

Jaynes, D. B., 1990, Soil water hysteresis: models and implications, *in* Anderson, M. G., and Burt, T. P., editors, Process Studies in Hillslope Hydrology: London, John Wiley and Sons Ltd., p. 93–126.

Jones, J. P., Sudicky, E. A., Brookfield, A. E., and Park, Y. J., 2006, An assessment of the tracer-based approach to quantifying groundwater contributions to streamflow: Water Resources Research, v. 42, W02407, doi:10.1029/2005WR004130.

Kirchner, J. W., 2003, A double paradox in catchment hydrology and geochemistry: Hydrological Processes, v. 17, p. 871–874.

——— 2006, Getting the right answers for the right reasons: linking measurements, analyses, and models to advance the science of hydrology: Water Resources Research, v. 42, WS03S04, doi: 10.1029/2005WR004362.

Kirkby, M. J., and Chorley, R. J., 1967, Throughflow, overland flow and erosion: Bulletin of the International Association of Scientific Hydrology, v. 12, p. 5–21.

Kitanidis, P. K., 1990, Effective hydraulic conductivity for gradually varying flow: Water Resources Research, v. 26, p. 1197–1208.

Klemes, V., 1986, Dilettantism in hydrology: Transition or destiny: Water Resources Research, v. 22, p. 177S–188S.

Kool, J. B., and Parker, J. C., 1987, Development and evaluation of closed-form expressions for hysteretic soil hydraulic properties: Water Resources Research, v. 23, p. 105–114.

Lamb, R., Beven, K. J., and Myrabø, S., 1998, Use of spatially distributed water table observations to constrain uncertainty in a rainfall-runoff model: Advances in Water Resources, v. 22, p. 305–317.

Lin, H., Bouma, J., Pachepsky, Y., Western, A., Thompson, J., van Genuchten, R., Vogel, H. J., and Lilly, A., 2006, Hydropedology: Synergistic integration of pedology and hydrology: Water Resources Research, v. 42, W05301, doi: 10.1029/2005WR004085.

Loague, K., and Green, R. E., 1991, Statistical and graphical methods for evaluating solute transport models: Overview and application: Journal of Contaminant Hydrology, v. 7, p. 51–73.

Loague, K., and VanderKwaak, J. E., 2002, Simulating hydrologic-response for the R-5 catchment: Comparison of two models and the impact of the roads: Hydrological Processes, v. 16, p. 1015–1032.

——— 2004, Physics-based hydrologic response simulation: Platinum bridge, 1958 Edsel, or useful tool: Hydrological Processes, v. 18, p. 2949–2956.

Loague, K., Heppner, C. S., Abrams, R. H., VanderKwaak, J. E., Carr, A. E., and Ebel, B. A., 2005, Further testing of the Integrated Hydrology Model (*InHM*): Event-based simulations for a small rangeland catchment located near Chickasha, Oklahoma: Hydrological Processes, v. 19, p. 1373–1398.

Loague, K., Heppner, C. S., Mirus, B. B., Ebel, B. A., Ran, Q., Carr, A. E., BeVille, S. H., and VanderKwaak, J. E., 2006, Physics-based hydrologic-response simulation: foundation for hydroecology and hydrogeomorphology: Hydrological Processes, v. 20, p. 1231–1237.

Merot, P., Ezzabar, B., Walter, C., and Aurousseau, P., 1995, Mapping waterlogging of soils using a digital terrain model: Hydrological Processes, v. 9, p. 27–34.

Merz, B., and Plate, E. J., 1997, An analysis of the effects of spatial variability of soil and soil moisture on runoff: Water Resources Research, v. 33, p. 2909–2922.

Mirus, B. B., Ebel, B., Loague, K., and Wemple, B. C., 2007, Simulated effect of a forest road on near-surface hydrologic response: Redux: Earth Surface Processes and Landforms, v. 32, p. 126–142.

Montgomery, D. R., ms, 1991, Channel initiation and landscape evolution: Berkeley, California, University of California, Berkeley, Ph. D. thesis, 421 p.

Montgomery, D. R., and Dietrich, W. E., 2002, Runoff generation in a steep, soil-mantled landscape: Water Resources Research, v. 38, p. 1168–1175.

Montgomery, D. R., Dietrich, W. E., Torres, R., Anderson, S. P., Heffner, J. T., and Loague, K., 1997, Hydrologic response of a steep, unchanneled valley to natural and applied rainfall: Water Resources Research, v. 33, p. 91–109.

Montgomery, D. R., Dietrich, W. E., and Heffner, J. T., 2002, Piezometric response in shallow bedrock at CB1: Implication for runoff generation and landsliding: Water Resources Research, v. 38, p. 1274–1292.

Nash, J. E., and Sutcliffe, J. V., 1970, River flow forecasting through conceptual models, Part I – A discussion of principles: Journal of Hydrology, v. 10, p. 282–290.

Rasmussen, T. C., 2001, Pressure wave vs. tracer velocities through unsaturated fractured rock: Geophysical Monograph, v. 42, p. 45–52.

Rodriguez-Iturbe, I., and Porporato, A., 2004, Ecohydrology of water-controlled ecosystems: Cambridge, United Kingdom, Cambridge University Press, 442 p.

Royer, J. M., and Vachaud, G., 1975, Field determination of hysteresis in soil-water characteristics: Soil Science Society of America Proceedings, v. 39, p. 221–223.

Saulnier, G. M., and Datin, R., 2004, Analytical solution to a bias in the TOPMODEL framework balance: Hydrological Processes, v. 18, p. 1195–1218.

Savenije, H. H. G., 2001, Equifinality, a blessing in disguise?: Hydrological Processes, v. 15, p. 2835–2838.

Schmidt, K. M., ms, 1999, Root strength, colluvial soil depth, and colluvial transport on landslide-prone hillslopes: Seattle, Washington, University of Washington, Seattle, Ph. D. thesis, 258 p.

Scott, P. S., Farquhar, G. J., and Kouwen, N., 1983, Hysteretic effects on net infiltration, *in* Advances in

infiltration, Publication 11-83: St. Joseph, Michigan, American Society of Agricultural Engineers, p. 163-170.

Seibert, J., and McDonnell, J. J., 2002, On the dialog between experimentalist and modeler in catchment hydrology: Use of soft data for multicriteria model calibration: Water Resources Research, v. 38, 1241, doi:10.1029/2001WR000978.

——— 2003, The quest for an improved dialog between modeler and experimentalist: Water Science and Application, v. 6, p. 301–315.

Si, B. C., and Kachanowski, R. G., 2000, Unified solution for infiltration and drainage with hysteresis: Theory and field test: Soil Science Society of America Journal, v. 64, p. 30–36.

Sidle, R. C., 2006, Field observations and process understanding in hydrology: essential components in scaling: Hydrological Processes, v. 20, p. 1439–1445.

Sidle, R. C., and Onda, Y., 2004, Hydrogeomorphology: overview of an emerging science: Hydrological Processes, v. 18, p. 597–602.

Stephenson, D. R., and Freeze, R. A., 1974. Mathematical simulation of subsurface flow contributions to snowmelt runoff, Reynolds Creek watershed, Idaho: Water Resources Research, v. 10, p. 284–294.

Torres, R., ms, 1997, Unsaturated zone processes and the hydrologic response of a steep, unchanneled valley: Berkeley, California, University of California, Berkeley, Ph. D. thesis, 298 p.

Torres, R., Dietrich, W. E., Montgomery, D. R., Anderson, S. P., and Loague, K., 1998, Unsaturated zone processes and the hydrologic response of a steep, unchanneled catchment: Water Resources Research, v. 34, p. 1865–1879.

Tromp-van Meerveld, H. J., and McDonnell, J. J., 2006, Threshold relations in subsurface stormflow: 2. The fill and spill hypothesis: Water Resources Research, v. 42, W02411, doi:10.1029/2004WR003800.

VanderKwaak, J. E., ms, 1999, Numerical simulation of flow and chemical transport in integrated surface-subsurface hydrologic systems: Waterloo, Ontario, Canada, University of Waterloo, Ph. D. thesis, 217 p.

VanderKwaak, J. E., and Loague, K., 2001, Hydrologic-response simulations for the R-5 catchment with a comprehensive physics-based model: Water Resources Research, v. 37, p. 999–1013.

van Genuchten, M. Th., 1980, A closed-form equation for predicting the hydraulic conductivity of unsaturated soils: Soil Science Society of America, v. 44, p. 892–898.

Vertessy, R. A., and Elsenbeer, H., 1999, Distributed modeling of storm flow generation in an Amazonian rain forest catchment: Effects of model parameterization: Water Resources Research, v. 35, p. 2173–2187.

Wealands, S. R., Grayson, R. B., and Walker, J. P., 2005, Quantitative comparison of spatial fields for hydrological model assessment – some promising approaches: Advances in Water Resources, v. 28, p. 15–32.

Weiler, M., and McDonnell, J., 2004, Virtual experiments: a new approach for improving process conceptualization in hillslope hydrology: Journal of Hydrology, v. 285, p. 3–18.

Whipkey, R. Z., 1965, Subsurface stormflow from forested slopes: Bulletin of the International Association of Scientific Hydrology, v. 10, p. 74–85.

Wigmosta, M. S., and Lettenmaier, D. P., 1999, A comparison of simplified methods for routing topographically-driven subsurface flow: Water Resources Research, v. 35, p. 255–264.

Wu, Y. S., Haukwa, C., and Bodvarsson, G. S., 1999, A site-scale model for fluid and heat flow in the unsaturated zone of Yucca Mountain: Journal of Contaminant Hydrology, v. 38, p. 185–215.

Yeh, T. C. J., and Harvey, D. J., 1990, Effective unsaturated conductivity of layered sands: Water Resources Research, v. 26, p. 1271–1279.